Inviscid instability of the Batchelor vortex: Absolute-convective transition and spatial branches

Cornel Olendraru and Antoine Sellier
LadHyX, CNRS–UMR 7646, École Polytechnique, F-91128 Palaiseau Cedex, France

Maurice Rossi
Laboratoire de Modélisation en Mécanique (LMM), Université Paris VI, Tour 66, 4, place Jussieu, F-75252 Paris cedex 05, France

Patrick Huerre
LadHyX, CNRS–UMR 7646, École Polytechnique, F-91128 Palaiseau Cedex, France

(Received 29 May 1998; accepted 5 March 1999)

The main objective of the study is to examine the spatio-temporal instability properties of the Batchelor q-vortex, as a function of swirl ratio q and external axial flow parameter a. The inviscid dispersion relation between complex axial wave number and frequency is determined by numerical integration of the Howard–Gupta ordinary differential equation. The absolute-convective nature of the instability is then ascertained by application of the Briggs–Bers zero-group-velocity criterion. A moderate amount of swirl is found to promote the onset of absolute instability. In the case of *wakes*, transition from convective to absolute instability always takes place *via* the helical mode of azimuthal wave number $m=-1$. For sufficiently large swirl, co-flowing wakes become absolutely unstable. In the case of *jets*, transition from absolute to convective instability occurs through various helical modes, the transitional azimuthal wave number m being negative but sensitive to increasing swirl. For sufficiently large swirl, weakly co-flowing jets become absolutely unstable. These results are in good qualitative and quantitative agreement with those obtained by Delbende *et al.*[1] through a direct numerical simulation of the linear response. Finally, the spatial (complex axial wave number, real frequency) instability characteristics are illustrated for the case of zero-external flow swirling jets. © *1999 American Institute of Physics.* [S1070-6631(99)04306-8]

I. INTRODUCTION

Swirling jets and wakes are encountered in many situations of current engineering interest. An understanding of their dynamics is for instance essential in the design of efficient combustors and in the control of trailing line vortices behind airplanes. Swirling jets and wakes are also ubiquitous in numerous atmospheric phenomena such as tornadoes, dust devils, and so forth. From a more fundamental standpoint, the evolution of swirling jets and wakes involves strong coupling between centrifugal forces associated with swirl, and Kelvin–Helmholtz instabilities associated with axial shear. Thus the dynamics of circular jets is profoundly altered by moderate levels of swirl: Helical instability modes of positive azimuthal wave number with respect to the applied swirl are very effectively quenched.[2–6] To the contrary, the centrifugally stable inertial modes of a pure vortex may be destabilized by axial shear, as demonstrated by Pedley[7,8] and Martin and Meiburg.[9]

The goal of the present investigation is to examine the properties of the spatio-temporal instability waves supported by the Batchelor[10] or q-vortex. We seek to determine the domains of absolute,[11,12] respectively convective, instability in parameter space by directly applying the Briggs–Bers[13,14] zero-group-velocity criterion to the inviscid dispersion relation. The characteristics of spatial waves (complex wave number, real frequency) are illustrated in a few typical instances. Preliminary results have been reported in Olendraru *et al.*[15] The study should be viewed as the analytical inviscid counterpart of the direct numerical simulation of the impulse response recently completed by Delbende *et al.*[1] for the same family of Batchelor velocity profiles.

The vortex breakdown phenomenon[16,17] exemplifies many of the subtleties involved in the dynamics of spatially developing swirling jets and wakes. The unsteady evolution is controlled simultaneously by the *local* instability properties of the underlying axial and azimuthal velocity profiles at each axial station, and by *global* constraints imposed on a large scale through upstream–downstream boundary conditions and the applied axial pressure gradient. Previous temporal instability analyses (real wave number, complex frequency) of parallel columnar vortices have sought to address the first issue. The second issue, namely global constraints in a finite-length pipe, has recently been considered by Wang and Rusak.[18]

It should be emphasized that local and global analyses are in fact strongly intertwined if one is willing to extend the local framework to spatio-temporal waves (complex wave number and frequency) and convective-absolute instability considerations. More specifically it has been demonstrated[11,19,20] that the existence of a finite region of local absolute instability promotes the onset of a global mode over an extended axial region. Furthermore, local spatio-temporal

waves constitute the buildings blocks of the linear global mode structure for slow variations of the vortex core along its axis, as in a tapered divergent duct configuration. In this context, Wang and Rusak's[18] instability calculations can be reduced to a combination of spatial waves and, as such, they provide an example of a linear global mode. In the absence of a region of local absolute instability, spatially developing flows act as spatial amplifiers of external noise. In such cases, the study of spatial waves is far more informative than a purely temporal analysis, since it fully documents the response of the flow to external forcing. To the authors' knowledge, all previous instability analyses of columnar vortices have been restricted to the temporal framework, with the exception of the recent papers by Delbende *et al.*[1] and Loiseleux *et al.*[6] It is our purpose here to examine spatio-temporal waves, as a first step towards a more comprehensive global mode formulation.

The Batchelor or q-vortex which is selected as basic flow is characterized by two nondimensional parameters: The swirl q associated with the azimuthal velocity distribution and the external flow a which controls the free-stream axial velocity (see Sec. II A). The Batchelor vortex is known to provide a satisfactory representation of slowly evolving trailing vortices as discussed by Batchelor,[10] Faler and Leibovich,[21] and Garg and Leibovich.[22] The latter authors have shown that this profile provides a good fit both to the jet-like flow upstream of vortex breakdown and to the wake-like flow downstream of breakdown. Sarpkaya[23] also found that it is a good approximation of the velocity field prevailing upstream of vortex breakdown. As the a-parameter is varied, the axial velocity profile evolves continuously from "jet-like" to "wake-like." In the vortex breakdown context, local axial velocity radial distributions are typically jet-like upstream of breakdown and wake-like downstream of breakdown. For temporal waves, the external flow parameter a may simply be removed by a Galilean transformation, i.e., by applying a trivial Doppler shift to the frequency. By contrast, a has a nontrivial effect on the absolute-convective nature of the instability as well as on the properties of spatial waves, and calculations have to be performed for all values of interest. As discussed in e.g., Huerre and Monkewitz,[11] it is precisely in situations where Galilean invariance is broken that absolute-convective instability issues acquire physical significance. This happens to be the case, either when the flow is continuously forced at a specific axial location, or when it is spatially developing, as for the slow vortex evolution in a divergent duct,[18] or else when the no-slip boundary condition is enforced at the walls. In such instances, the pertinent reference frame is unambiguously defined. In the present analysis, it is therefore crucial to keep as independent parameters both the swirl q and the external axial flow a.

The inviscid temporal instability of swirling jets and wakes typically reduces to a classical eigenvalue problem expressed in terms of the second-order Howard-Gupta[24] ordinary differential equation. The main results for the Batchelor vortex[5,25] may be summarized as follows. For zero swirl, the q-vortex is in effect a fully developed Gaussian jet and only the bending modes of azimuthal wave number $m=\pm 1$ are unstable where m is defined in the normal mode form (3). When q exceeds 0.08, all positive helical modes ($m>0$) become stable. For moderate swirl values, negative helical modes ($m<0$) are, however, strongly destabilized, with growth rates typically an order of magnitude larger than for a nonrotating jet. In Delbende *et al.*[1] and Loiseleux *et al.*[6] it was erroneously stated that the Batchelor vortex becomes linearly stable above $q\sim 1.5$. This is only valid for a particular subclass of inviscid modes. According to Stewartson and Brown's[26] asymptotic study, some inviscid modes remain unstable at high q within specific ranges of swirl. To the present day, these findings have not been confirmed numerically. The precise neutral boundary is difficult to determine accurately: According to Leibovich and Stewartson,[27] inviscid instability modes with identical axial and azimuthal wave numbers coalesce near neutrality, which impedes the convergence of numerical algorithms. In the unstable swirl range, the maximum growth rate monotonically increases with $|m|$ and reaches a finite value for $m=-\infty$. The maximum growth rate over all axial and azimuthal wave numbers is reached at $q=0.87$. The effect of viscosity has been examined by Lessen and Paillet,[3] Khorrami,[28] and Mayer and Powell.[25] These investigations have demonstrated the existence of distinct unstable viscous modes, with growth rates several orders of magnitude lower than their inviscid counterparts. In the present investigation, such modes are *de facto* not considered since the analysis is purely inviscid.

The absolute-convective instability of swirling jets and wakes has only recently been examined.[1,6] In the numerical study of Delbende *et al.*,[1] the linear impulse response of the Batchelor vortex is simulated at the particular Reynolds number $\mathrm{Re}=667$ in order to determine whether it grows *in situ* (absolute instability) or is convected downstream (convective instability). The introduction of a moderate amount of swirl is found to strongly promote absolute instability without necessarily requiring the presence of a finite counterflow. The present study examines the same questions from an alternative point of view, by directly solving the inviscid dispersion relation and applying the Briggs–Bers[13,14] zero-group- velocity criterion. Since both methods lead to very similar conclusions, the discussion of the results is postponed to Sec. VI. The Briggs–Bers criterion has also been applied by Loiseleux *et al.*[6] to the analytically derived inviscid dispersion relation of the Rankine vortex with superimposed axial plug flow. Here again, the results indicate that absolute instability is strongly enhanced by swirl: Co-flowing jets and wakes may become absolutely unstable for moderate amounts of swirl.

The application of the absolute-convective instability formulation to swirling flows may be regarded as the logical extension of the group velocity concept first introduced by Benjamin[29] and Tsai and Widnall[30] in the context of vortex breakdown. Benjamin's[29] criterion is based on the computation of the phase velocity pertaining to long-wavelength axisymmetric neutral disturbances. In this limit, waves are nondispersive so that phase and group velocities coincide. As the ratio of basic azimuthal to axial velocities is varied, such disturbances are determined to propagate either solely in the downstream direction (supercritical flow) or both upstream and downstream (subcritical flow). Vortex breakdown is then

viewed as a transition between a supercritical state and a downstream subcritical state. However, pertinent it may be for vortex breakdown, this analysis is incomplete: (a) It does not consider *dispersive* and *unstable helical* waves such as bending ($m=\pm 1$) or higher-order azimuthal modes; (b) it does not examine arbitrary wavelengths. These restrictions were partly removed by Tsai and Widnall[30] for the vortex flow in a divergent duct undergoing breakdown. The notions of supercritical and subcritical flow states were redefined with respect to the group velocity of neutral dispersive waves of finite wavelength. Note, however, that the dispersive wave propagation characteristics may be obtained analytically for arbitrary profiles and arbitrary azimuthal wave number m in the long wavelength approximation as demonstrated by Leibovich *et al.*[31] An absolute-convective instability analysis precisely provides the logical framework to extend the notions of supercritical (i.e., convectively unstable) and subcritical (i.e., absolutely unstable) flow states by examining the propagation of unstable disturbances of arbitrary axial and azimuthal wave numbers.

The paper is organized as follows. The basic flow and the eigenvalue problem to be solved are defined in Secs. II A and II B, respectively. Sec. II C considers the asymptotic behavior of disturbances near the axis and near infinity, and the required contour deformation rule around critical points of the Howard–Gupta equation. The numerical procedure leading to the dispersion relation between wave number and frequency is outlined in Sec. II D. In Sec. III, we discuss the absolute-convective nature of the instability in the plane of control parameters a and q. The characteristics of spatial waves are illustrated in Sec. IV for the case of zero external flow swirling jets. Typical spatial eigenfunctions in the convectively unstable range are presented in Sec. V. The main results are summarized and compared with related studies in Sec. VI.

II. LINEAR INVISCID INSTABILITY FORMULATION

A. Basic flow

As in Olendraru *et al.*[15] and Delbende *et al.*,[1] the basic swirling flow under consideration is taken to be the Batchelor[10] or q-vortex. Let x, r, and θ denote the usual axial, radial, and azimuthal coordinates, and U, V, W the corresponding basic velocity components. The Batchelor vortex flow is then given by the two-parameter family

$$U(r)\equiv a+e^{-r^2}, \quad V(r)\equiv 0, \quad W(r)\equiv q[1-e^{-r^2}]/r. \tag{1}$$

The above relations have been made nondimensional by selecting as length scale the vortex core size R, and as velocity scale the difference $\Delta U\equiv U_c-U_\infty$ between the centerline axial velocity U_c on the $r=0$ axis and the free-stream velocity U_∞ at $r=\infty$. If Ω_c denotes the core rotation rate, the nondimensional external flow parameter a and swirl parameter q are defined as

$$a\equiv\frac{U_\infty}{\Delta U}, \quad q\equiv\frac{\Omega_c R}{\Delta U}. \tag{2}$$

In other words, a and q, respectively, provide a measure of free-stream axial velocity and maximum core swirl velocity. Typical azimuthal and axial velocity profiles are represented in Fig. 1 for increasing values of q and a. By increasing a, one may successively study co-flowing wakes [$(a<-1$, Fig. 1(b)], counter-flowing jets or wakes [$-1<a<0$, Fig. 1(c)], and co-flowing jets [$a>0$, Fig. 1(d)]. The zero-external flow jet is recovered for $a=0$, and the zero center line velocity wake is obtained for $a=-1$. In the $a-q$ parameter plane, the half planes $a>-0.5$ and $a<-0.5$ will be referred to as the "jet" side and "wake" side, respectively. Note that in the context of the present inviscid analysis, (1) is an admissible basic flow since it is a solution of the Euler equations.

B. Eigenvalue problem

The analysis is restricted to the evolution of infinitesimal disturbances superimposed on the basic flow field (1). The flow is assumed to be inviscid and incompressible of constant density. Since the basic flow is parallel and steady, nondimensional velocity and pressure fluctuations may be decomposed into normal modes of the form

$$(u,v,w,p)=\mathrm{Re}\{[F(r),iG(r),H(r),P(r)]e^{i(kx+m\theta-\omega t)}\}, \tag{3}$$

where the azimuthal wave number m is an integer, and the axial wave number k and frequency ω may be complex. As shown by Batchelor and Gill[32] for the pure jet case ($q=0$) and Lessen *et al.*[5] for swirling jets, substitution of Eq. (3) into the Euler equations linearized around the basic state (1), leads to the first-order system

$$krF+(rG)'+mH=0, \tag{4a}$$

$$\gamma G+2WH/r-P'=0, \tag{4b}$$

$$\gamma rH+(rW)'G+mP=0, \tag{4c}$$

$$\gamma F+U'G+kP=0. \tag{4d}$$

In the above relations a prime denotes differentiation with respect to r and

$$\gamma(r)\equiv kU(r)-\omega+mW(r)/r. \tag{5}$$

To this system, one must add the usual exponential decay boundary conditions at $r=\infty$ and require that physical quantities remain smooth, bounded, and single-valued on the $r=0$ axis. As discussed in detail in Batchelor and Gill,[32] the boundary conditions appropriate to system (4) take the form

$$F(\infty)=G(\infty)=H(\infty)=P(\infty)=0 \quad \text{for all } m, \tag{6a}$$

$$F(0)=G(0)=H(0)=P(0)=0 \quad \text{if } m^2>1, \tag{6b}$$

$$G(0)=H(0)=0, \quad F(0) \text{ and } P(0) \text{ finite if } m=0, \tag{6c}$$

$$H(0)\pm G(0)=0, \quad F(0)=P(0)=0 \quad \text{if } m=\pm 1. \tag{6d}$$

As noticed by Howard and Gupta,[24] it is actually possible to recast system (4) into a single second-order boundary-value problem for the function $Z(r)\equiv rG(r)/\gamma(r)$. After elementary manipulations, one is led to the system derived by Howard and Gupta[24]

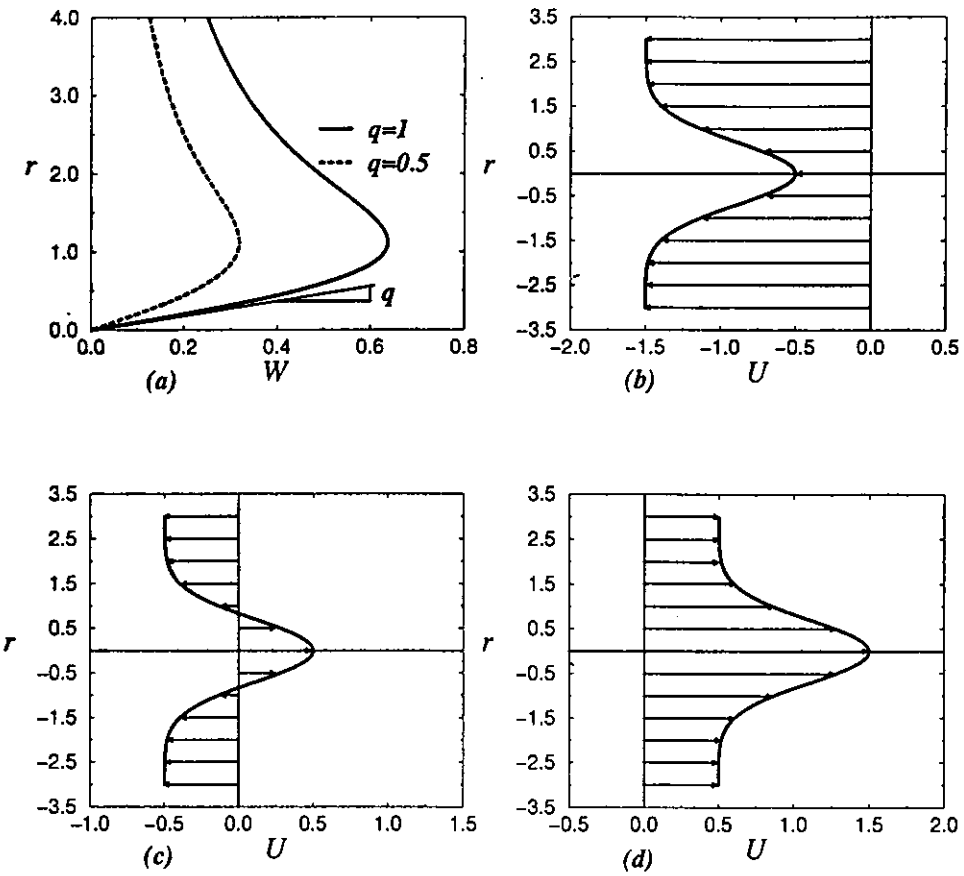

FIG. 1. Batchelor vortex velocity field. (a): Azimuthal velocity profile $W(r)$ for $q=0.5$ and $q=1.0$. Axial velocity profile $U(r)$ for (b): Co-flowing wakes if $a<-1$; (c): counter-flowing wakes/jets if $-1<a<0$; (d): co-flowing jets if $a>0$.

$$r^2\gamma^2(m^2+k^2r^2)Z''+[(m^2-k^2r^2)r\gamma^2 +2(m^2+k^2r^2)r^2\gamma\gamma']Z'-[\gamma^2(m^2+k^2r^2)^2 +2(m^2+k^2r^2)mr\gamma(W/r)'-4mk^2r\gamma W -2kW(m^2+k^2r^2)(k(rW)'-mU')]Z=0, \tag{7}$$

$$Z(0)=Z(\infty)=0. \tag{8}$$

The two-point boundary value problem (7), (8) is in effect an eigenvalue problem: For given control parameter settings (m,a,q), nontrivial solutions Z exist if and only if the complex frequency ω and the axial wave number k are linked by a dispersion relation of the form

$$D[k,\omega;m,a,q]=0. \tag{9}$$

Note that the eigenvalue problem (7), (8) being invariant under the transformation $q\to -q$, $m\to -m$, the same property holds for the dispersion relation (9). Unless otherwise stated, we restrict the study to $q\geqslant 0$ with m a positive or negative integer. Corresponding results for $q\leqslant 0$ may readily be obtained by changing q into $-q$ and m into $-m$.

C. Asymptotic behavior near $r=0$ and $r=\infty$ and critical point singularity

In order to solve numerically system (7), (8) by a shooting method, it is essential to examine the asymptotic behavior of the solutions near the axis $r=0$ and at $r=\infty$, and to properly account for the critical point singularity r_c defined by $\gamma(r_c)=0$.

To investigate the *behavior of* $Z(r)$ *near* $r=0$, it is assumed that $\gamma(0)=k(a+1)-\omega+mq\neq 0$, i.e., that $r=0$ is not a critical point of the ordinary differential equation [Eq. (7)]. In the present spatio-temporal study, k or/and ω are complex and this assumption has been found to always hold. Under this condition, it is straightforward to apply the method of Frobenius (Bender and Orszag[33]) to ordinary differential equation [Eq. (7)] near $r=0$ and to enforce boundary condition (8). The following results are then obtained:

When $m=0$,

$$Z(r)=r^2[1+br^2+\mathcal{O}(r^3)], \quad \frac{Z'}{Z}=\frac{1}{r}[2+3br^2+\mathcal{O}(r^3)], \tag{10}$$

where

$$b\equiv\frac{k^2}{8}\left[1-\frac{4q^2}{\gamma^2(0)}\right]+\frac{k}{\gamma(0)}. \tag{11}$$

When $|m|\geqslant 1$

$$Z(r)=r^{|m|}[1+dr^2+\mathcal{O}(r^3)], \quad \frac{Z'}{Z}=\frac{1}{r}[|m|+(|m|+1)dr^2+\mathcal{O}(r^3)], \tag{12}$$

where

$$4(|m|+1)d\equiv k^2\left[1+\frac{2}{|m|}-\frac{4q}{m\gamma(0)}-\frac{4q^2}{\gamma^2(0)}\right]+\frac{4k}{\gamma(0)}\left[|m|-\frac{mq}{\gamma(0)}\right]+\frac{2m(|m|-1)q}{\gamma(0)}. \tag{13}$$

The *behavior of* $Z(r)=rG(r)/\gamma(r)$ *near* $r=\infty$ may be inferred by first noticing that

$$\frac{Z'}{Z}=\frac{G'}{G}+\frac{1}{r}-\frac{\gamma'}{\gamma}. \tag{14}$$

According to Lessen *et al.*[5] and Ash and Khorrami,[2] for large r

$$G\sim-\frac{F'}{k}, \tag{15}$$

whence

$$\frac{Z'}{Z}\sim\frac{F''}{F}+\frac{1}{r}-\frac{\gamma'}{\gamma}. \tag{16}$$

The asymptotic behavior of Z'/Z may therefore be deduced from that of F. In the free stream, for large r, $F(r)$ satisfies the modified Bessel equation

$$F''+\frac{F'}{r}-\frac{k^2r^2+m^2}{r^2}F=0. \tag{17}$$

Assume, without loss of generality (Huerre and Monkewitz[34]), that the wave number is restricted to the right-hand complex k-plane $k_r=\mathrm{Re}\,k>0$. The only solution of Eq. (16) that vanishes at $r=\infty$ to comply with Eq. (6a) is then of the form $F(r)=K_{|m|}(kr)$, where $K_\nu(u)$ is the modified Bessel function of the second kind (Abramovitz and Stegun[35]). Upon substituting this solution into Eq. (16), invoking Eq. (17) and making use of standard recursive relations pertaining to K_ν and its derivative, one is led to the following asymptotic results for large r:

When $m=0$,

$$\frac{Z'}{Z}\sim-k\frac{K_0(kr)}{K_1(kr)}. \tag{18}$$

When $|m|\geqslant 1$,

$$\frac{Z'}{Z}\sim\frac{2mq}{mqr+(ka-\omega)r^3}-\frac{k[1+m^2/(k^2r^2)]K_{|m|}(kr)}{(m/kr)K_{|m|}(kr)+K_{|m|-1}(kr)}. \tag{19}$$

The second-order differential equation [Eq. (7)] displays regular singular points (Bender and Orszag[33]) or so-called critical points r_c at complex r locations such that $\gamma(r_c)=0$. The present inviscid analysis breaks down in the vicinity of critical points. Furthermore, by analogy with the large Reynolds number asymptotic theory of the Orr–Sommerfeld equation (Lin,[36] Wasow,[37] Drazin and Reid[38]), the inviscid solutions of Eq. (7) are expected, in the limit of vanishing viscosity, to become invalid approximations to their viscous counterparts in specific "viscous" sectors emerging from r_c in the complex r-plane. In the process of solving Eq. (7), one must, therefore, select an integration path in the complex r-plane that scrupulously avoids the viscous sectors emerging from r_c, so as to preserve the validity of the inviscid approach. A contour deformation rule analogous to the Rayleigh–Orr–Sommerfeld equation case has been proposed by Lessen *et al.*[5] in the strictly temporal (k real, ω complex) framework: *If there exist a complex critical point* r_c *such that* $\gamma(r_c)=0$ *with* $\gamma'(r_c)\neq 0$, *the original integration path along the real r axis may have to be deformed in order to lie below* r_c *when* $\mathrm{Re}\,\gamma'(r_c)>0$ *and above* r_c *when* $\mathrm{Re}\,\gamma'(r_c)<0$. Under this condition, the integration path does not cross the viscous sector located in the upper half-plane $\mathrm{Im}\,r\geqslant\mathrm{Im}\,r_c$ (respectively, lower half-plane $\mathrm{Im}\,r\leqslant\mathrm{Im}\,r_c$). The inviscid eigenvalues thus obtained are then ensured to be the limits of their viscous counterparts as the viscosity tends to zero. The generalization of the contour deformation rule to arbitrary complex values of k and ω of interest here is highly nontrivial, even in the Rayleigh–Orr–Sommerfeld case recently examined by Le Dizès *et al.*[39] According to Fig. 1 of Le Dizès *et al.*,[39] the critical point y_c of the Rayleigh equation, which lies on the real y axis for neutral waves (k and ω real) gradually moves into the complex y plane as k and ω become complex. Concurrently, the viscous sector of angle $2\pi/3$ issuing from y_c, which for neutral waves is located entirely in the upper or lower half y plane, experiences a rotation of angle $\arg k/3$. Thus, for sufficiently moderate values of $k_i\equiv\mathrm{Im}\,k$ and $\omega_i\equiv\mathrm{Im}\,\omega$, the viscous sector safely remains in the same half-plane above or below y_c and it is legitimate to use the *same* contour deformation rule as for temporal waves (k real, ω complex). We assume that a similar reasoning remains valid for instability waves in swirling flows: *The contour deformation rule of* Lessen *et al.*[5] *is presumed to hold for k and* ω *complex.* Note that the same path deformation rule follows by invoking causality within a strictly inviscid framework (Case[40]): For purely spatial waves (ω real, k complex) real frequencies should be approached by letting their imaginary part tend to zero from positive values. This requirement results in identical prescriptions.

As shown in the Appendix, the equation $\gamma(r)=0$ gives rise, for the Batchelor velocity profiles (1), to zero, one or two nonzero complex critical points $r_{c,1}$ and $r_{c,2}$ with $\mathrm{Re}\,r_c\geqslant 0$.

This completes the examination of the properties of system (7), (8) necessary to numerically determine the complex solutions of dispersion relation (9).

D. Numerical procedure

Equation (7) may be rewritten as the following first-order system for $Z(r)$ and $Y(r)=dZ/dr$:

$$Z'=Y, \tag{20a}$$

$$Y'=-\left[\frac{1}{r}+\frac{2\gamma'}{\gamma}-\frac{2k^2r}{m^2+k^2r^2}\right]Y+\left[\frac{m^2+k^2r^2}{r^2}+\frac{2m}{\gamma r}\left(\frac{W}{r}\right)'-\frac{4mk^2W}{\gamma r(m^2+k^2r^2)}-\frac{2kW}{\gamma^2r^2}(k(rW)'-mU')\right]Z. \tag{20b}$$

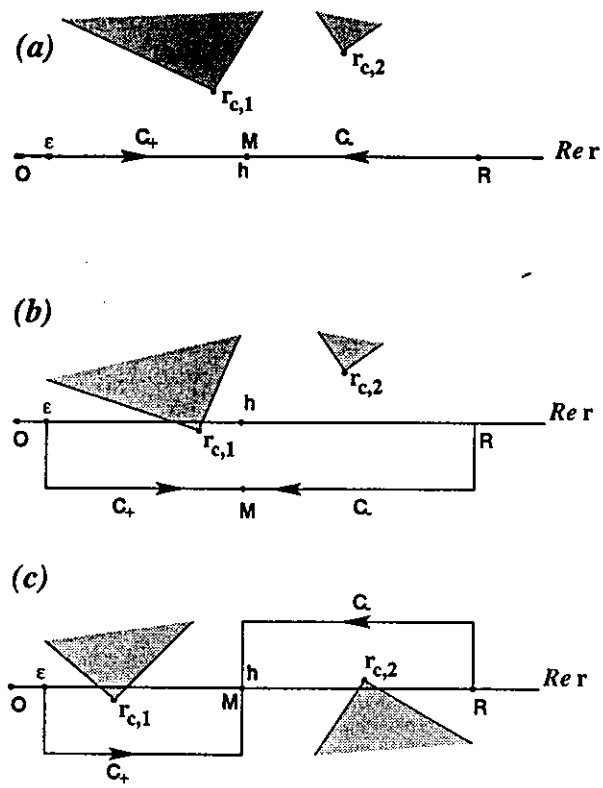

FIG. 2. Contour deformation rule in complex r plane; viscous sectors are indicated in gray. (a): $\mathrm{Im}\, r_{c,j}\, \mathrm{Re}[\gamma'(r_{c,j})]>0$, $j=1,2$, purely real integration paths C_- and C_+. (b): $\mathrm{Im}\, r_{c,1}<0$, $\mathrm{Re}[\gamma'(r_{c,1})]>0$; $\mathrm{Im}\, r_{c,2}>0$, $\mathrm{Re}[\gamma'(r_{c,2})]>0$, integration paths C_- and C_+ located in same lower half r plane. (c): $\mathrm{Im}\, r_{c,1}<0$, $\mathrm{Re}[\gamma'(r_{c,1})]>0$; $\mathrm{Im}\, r_{c,2}>0$, $\mathrm{Re}[\gamma'(r_{c,2})]<0$, integrations paths C_- and C_+ located in lower and upper half r planes, respectively.

Such a system is to be solved for given parameter settings (m, a, q), subject to the conditions that $Y/Z=Z'/Z$ behaves as Eqs. (10) or (12) for small r, and as Eqs. (18) or (19) for large r. Consider two real numbers $\epsilon \ll 1$ and $R \gg 1$, respectively, small and large enough to apply the near-axis approximation formulas (10) or (12) for $Z'(\epsilon)/Z(\epsilon)$, and the far-field approximation formulas (18) or (19) for $Z'(R)/Z(R)$. A natural procedure then consists in integrating system (20) on the real r axis, from $r=\epsilon$ and $r=R$ toward a common real matching point $r=h$ with $\epsilon<h<R$. As sketched in Fig. 2(a), this approach amounts to matching in the complex r plane along two straight line segments C_- and C_+ that lie on the real r axis and meet at $r=h$. For arbitrary values of k and ω, two distinct values of $Z'(h^-)/Z(h^-)$ and $Z'(h^+)/Z(h^+)$ are thereby generated on either side of the matching point $r=h$. In order for a complex pair (k,ω) to be a solution of the dispersion relation (9), the associated Wronskian

$$W(k,\omega;m,a,q)\equiv Z'(h^+)Z(h^-)-Z(h^+)Z'(h^-) \qquad (21)$$

must vanish. In practice, a realistic guess value (k_G,ω_G) is specified and the Wronskian W is numerically brought to zero by changing one of the elements in the complex pair (k,ω) via a Newton–Raphson algorithm.

From the discussion of Sec. II C, integration along the real r axis, as described above, is legitimate only when there are no critical points, or the viscous sectors issuing from the critical points $r_{c,1}$ and $r_{c,2}$, remain entirely within the same half r plane as $r_{c,1}$ and $r_{c,2}$ without ever being crossed by the real r axis, as in Fig. 2(a). According to the contour deformation rule of Lessen *et al.*,[5] such a real integration path holds either when $\mathrm{Re}\, r_{c,j} \gg R$, $j=1,2$ (critical points lying outside the integration domain), or when $\mathrm{Im}\, r_{c,j}\, \mathrm{Re}\, \gamma'(r_{c,j})>0$ for both $j=1$ and $j=2$ [viscous sectors located in same upper or lower half r plane as $r_{c,j}$, Fig. 2(a)]. In all other cases, integration must proceed along a rectangular path in the complex r plane that complies with the contour deformation rule in order to avoid the viscous sectors. Typical situations are illustrated in Figs. 2(b) and 2(c). If $\mathrm{Im}\, r_{c,1}<0$, $\mathrm{Re}\, \gamma'(r_{c,1})>0$ and $\mathrm{Im}\, r_{c,2}>0$, $\mathrm{Re}\, \gamma'(r_{c,2})>0$, the configuration shown in Fig. 2(b) holds: The contours C_+ and C_- are then chosen to lie in the lower half r plane at an elevation $\mathrm{Im}\, r=-\delta$ and the matching point M where the Wronskian (21) has to be brought to zero, is taken to be at $r=h-i\delta$, $\delta>0$. If $\mathrm{Im}\, r_{c,1}<0$, $\mathrm{Re}\, \gamma'(r_{c,1})>0$ and $\mathrm{Im}\, r_{c,2}>0$, $\mathrm{Re}\, \gamma'(r_{c,2})<0$, the configuration shown in Fig. 2(c) holds: The contours C_+ and C_- are chosen to lie in the lower and upper half r plane, at elevations $\mathrm{Im}\, r=-\delta$ and $\mathrm{Im}\, r=\delta$, respectively, and the matching point M remains on the real r axis at $r=h$.

The above numerical procedure is practically implemented by resorting to readily available IMSL routines, as in Pavithran and Redekopp.[41] If the integration is to be performed along complex contours such as those in Fig. 2(b) and 2(c), an appropriate change of variable r is applied to system (20). The IMSL routine DIVPAG is then used to integrate the first-order system from $r=\epsilon$ and $r=R$ to the matching point M located at $r=h$ [Figs. 2(a) and 2(c)] or $r=h-i\delta$ [Fig. 2(b)]. A value of the Wronskian (21) is thereby generated for a given complex pair (k,ω). The IMSL routine DNEQNF is then used to bring the Wronskian W to zero via a Newton–Raphson algorithm. Realistic guess values (k_G,ω_G) are inferred by exploiting the temporal results of Lessen *et al.*[5] as described at the end of this section. The location of potential critical points $r_{c,1}$ and $r_{c,2}$ such that $\mathrm{Re}\, r_{c,j}\geqslant 0$ and $\gamma(r_{c,j})=0$ is estimated by applying the Newton–Raphson DNEQNF routine to the complex function γ. Critical points for the bending modes $m=\pm 1$ are readily deduced by continuation from the zero-swirl case $q=0$. The guess value $r_{G,c}=1$ is chosen as input for all higher-order helical modes $|m|>1$. In a few instances, convergence failed, which indicated the presence of another critical point, as discussed in Sec. IV.

Numerical calculations were performed with $\epsilon=10^{-3}$ and $R=15$. Khorrami *et al.*[42] note that the value $R=3$ selected by Lessen *et al.*[5] is somewhat low. The present value $R=15$ was deemed to be sufficiently large for the asymptotic estimates (18), (19) of Z'/Z to remain valid over a wide range of the complex argument kR. Finally, for most runs, the elevation of the deformed contours was chosen to be $\delta=10^{-1}$.

When a converged eigenvalue pair has been obtained, the corresponding eigenfunction is easily retrieved by performing one last integration run of the system (20) for $Z(r)$ and $Z'(r)$, along the *real* r axis from $r=\epsilon$ to $r=R$. Accord-

ing to the original first-order system (4), the eigenfunctions F, G, H, and P for all physical quantities are then calculated from the following relations:

$$F=\frac{\{(m/r)[k(rW)'-mU']-kr\gamma'\}Z-\gamma krZ'}{m^2+k^2r^2}, \tag{22}$$

$$G=\frac{\gamma}{r}Z, \tag{23}$$

$$H=\frac{\{k[mU'-k(rW)']-m\gamma'\}Z-\gamma mZ'}{m^2+k^2r^2}, \tag{24}$$

$$P=\frac{\gamma}{m^2+k^2r^2}\left[\left\{r\gamma'-\frac{1}{r}[kr^2U'+m(rW)']\right\}Z+r\gamma Z'\right]. \tag{25}$$

The radial distribution of F, G, H, and P computed in this manner remain uniform approximations of the true eigenfunctions as long as there is no critical point on the real r axis and the viscous sectors of Fig. 2 do not contaminate part of the real r axis. If this is not the case, the computed eigenfunctions are only valid large-Reynolds-number approximations outside the viscous sectors.

The present investigation relies in large measure on the effective calculation of generalized spatial branches whereby ω is assigned a given real or complex value and $k(\omega)$ is a complex unknown. Spatial branches in the strict sense then correspond to ω real and k complex. In all cases, a realistic guess value (k_G,ω) is needed in order to initiate the Newton–Raphson algorithm and to ensure successful convergence to an eigenvalue pair (k,ω). Such guess values are inferred from the temporal results of Lessen *et al.*:[5] A known temporally growing mode (k real, ω complex) with $\omega_i>0$ is used as a starting point to generate by continuation a spatial branch $k(\omega)$ for the same value of ω_i and varying values of ω_r. In other words, the locus of the spatial branch $k(\omega)$ is effectively represented in the complex k plane as a level curve $\omega_i=\text{const}$. Level curves for successively increasing and decreasing values of ω_i are also obtained by continuation. The particular level curve $\omega_i=0$ then corresponds to the conventional spatial branch k complex, ω real. The numerical code is found to experience convergence difficulties in the vicinity of neutral conditions (k real, ω real) as expected from the analyses of Leibovich and Stewartson[27] and Mayer and Powell[25] (see Sec. I). The Newton–Raphson algorithm is then prone to skipping from one mode to another.

III. ABSOLUTE-CONVECTIVE NATURE OF THE INSTABILITY

The absolute-convective nature of each azimuthal wave number m is ascertained by analyzing the behavior of spatial branches $k(\omega;m,a,q)$ in the vicinity of saddle points (k_0,ω_0) of the dispersion relation (9) for given settings of the swirl q and external flow parameter a. The reader is referred to Huerre and Monkewitz[11] for a survey of these concepts and to Huerre and Rossi[12] for a detailed presentation. According to the criterion established by Briggs[13] and Bers,[14] saddle points $[k_0(m,a,q),\omega_0(m,a,q)]$ of the dispersion relation (9) are formally defined by imposing the zero-group-velocity condition

$$\frac{\partial\omega}{\partial k}(k_0;m,a,q)=0, \quad \omega_0=\omega(k_0;m,a,q). \tag{26}$$

Pertinent saddle points necessarily involve pinching of two distinct spatial branches $k^+(\omega;m,a,q)$ and $k^-(\omega;m,a,q)$ which, for large enough $\omega_i>0$, are entirely located in the distinct half k-planes $k_i>0$ and $k_i<0$, respectively. If this essential pinching condition is satisfied, k_0, and ω_0 qualify as the complex absolute wave number and frequency, respectively, the quantity $\omega_{0,i}\equiv\text{Im}\,\omega_0$ denoting the absolute growth rate. When $\omega_{0,i}>0$, the basic flow is said to be absolutely unstable [absolute instability (AI)] for the particular m under consideration. When $\omega_{0,i}<0$, it is convectively unstable [convective instability (CI)] for azimuthal wave number m. For given m, the AI–CI transition curve in $a-q$ space is formally given by $\omega_{0,i}(m,a,q)=0$. In order to determine the overall AI–CI transition curve, the above reasoning must be repeated for different values of m. The strictly spatial approach (k complex, ω real) is known to be pertinent only when the flow is CI: The spatial branches $k^+(\omega;m,a,q)$ and $k^-(\omega;m,a,q)$ are then associated with the "right-hand side" ($x>0$) and "left-hand side" ($x<0$) response to a time-harmonic excitation of frequency ω located at $x=0$ (signalling problem). More specifically, in the case of *jets* [$a>-0.5$, Fig. 1(d)], the flow is predominantly directed to the right: k^+ and k^- are then conveniently referred to as the "downstream" ($x>0$) and "upstream" branch ($x<0$), respectively. A contrario, in the case of *wakes* [$a<-0.5$, Fig. 1(b)], the flow is predominantly directed to the left: k^+ and k^- then switch denominations and become the upstream ($x>0$) and downstream ($x<0$) branch, respectively.

Since the AI–CI transition curve is defined by the real absolute frequency condition $\omega_{0,i}(m,a,q)=0$, it is natural to seek its determination by resorting to a straightforward spatial approach (k complex, ω real). As discussed for instance in Huerre and Rossi,[12] in the purely spatial instability context, an AI–CI transition point is signalled by the appearance of a cusp singularity in the curves of spatial growth rate $-k_i^+(\omega;m,a,q)$ and wave number $k_r^+(\omega;m,a,q)$ versus real frequency ω. For given settings of q and m, we therefore, choose to detect the presence of a cusp singularity in the spatial instability characteristics as the external flow parameter a is varied.

A typical example is illustrated in Fig. 3 for the $m=\pm1$ modes in the case of a zero-swirl ($q=0$) jet: As a decreases from $a=-0.35$ to $a=-0.37$ (increasing external counterflow $|a|$), the spatial growth rate curve $-k_i^+(\omega;m,a,q)$ gradually exhibits a cusp singularity at the real absolute frequency $\omega_{0,r}\sim0.04$. A more accurate evaluation yields $a_t^j=-0.371$, where the j superscript stands for the "jet side" AI–CI transition point. It can subsequently be checked that at the parameter values $m=\pm1$, $a_t^j=-0.371$, $q=0$, the real frequency $\omega_{0,t}$ giving rise to the cusp is indeed associated with pinching of distinct spatial branches k^+ and k^- at the saddle point k_0: Isocontour levels $\omega_i=\text{const}$. cor-

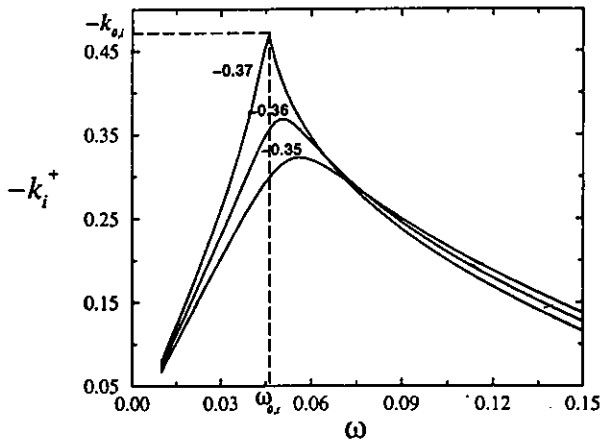

FIG. 3. Effect of increasing external counterflow $|a|$ on the spatial instability characteristics of zero-swirl ($q=0$) jets: Spatial growth rate $-k_i^+$ of helical modes $m=\pm 1$ versus real frequency ω, as external flow parameter decreases from $a=-0.35$ to $a=-0.37$. Note appearance of cusp for $a=-0.37$ at $\omega_{0,r}\sim 0.04$, $-k_{0,i}\sim 0.5$.

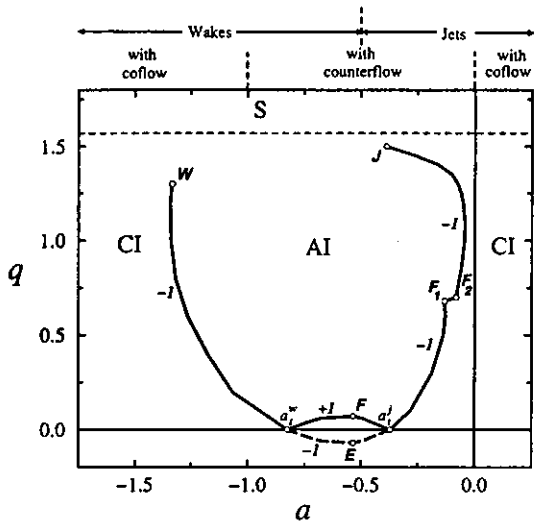

FIG. 5. AI–CI nature of helical mode $m=-1$. Domains of stability (S), convective instability (CI), and absolute instability (AI) in $a-q$ parameter plane. Curve WEF_1F_2J indicates AI–CI transition curve of mode $m=-1$. Curve $a_t^wFa_t^j$ indicates AI–CI transition curve of mode $m=1$.

responding to the k^+ and k^- branches are displayed in Fig. 4. As ω_i decreases to zero, both sets of curves pinch at the saddle point k_0. As ω_i increases above zero, they gradually recede into their respective half-planes $k_i>0$ and $k_i<0$, thereby satisfying the Briggs–Bers criterion. A genuine pinching point has, therefore, been found for a real absolute frequency ($\omega_{0,i}=0$). Thus, for zero swirl $q=0$, $a_t^j=-0.371$ is indeed an AI–CI transition point of helical modes $m=\pm 1$. A similar procedure may be used to determine the AI–CI nature of the same helical modes $m=\pm 1$, for other values of the external flow parameter a on the line $q=0$ (see Fig. 5). By drawing contour maps similar to those of Fig. 4, one may establish the following results: When $a>a_t^j$, the pinching point k_0 ($m=\pm 1$, a, $q=0$) persists, but it is now obtained for a negative absolute growth rate $\omega_{0,i}$ ($m=\pm 1$, a, $q=0)<0$, thereby indicating that the flow is CI. Conversely, in the range $a_t^w<a<a_t^j$, where $a_t^w\equiv -0.825$ refers to a second AI–CI transition value on the wake side, $\omega_{0,i}$ ($m=\pm 1$, a, $q=0)>0$ and the flow is AI. Finally, when $a<a_t^w$, $\omega_{0,i}$ ($m=\pm 1$, a, $q=0)<0$ and the flow returns to CI.

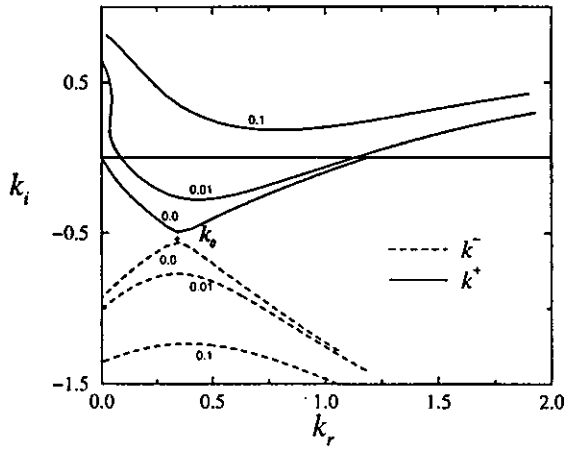

FIG. 4. Illustrative loci of spatial branches $k(\omega)$ in complex k plane for $m=\pm 1$, $a=a_t^j=-0.371$, $q=0$. Level curves $\omega_i=0.1$, $\omega_i=0.01$, $\omega_i=0.00$. Solid lines: $k^+(\omega)$; dashed lines: $k^-(\omega)$. Note pinching of k^+ and k^- branches at k_0 as ω_i decreases to zero.

The same methodology may be applied for successively increasing values of the swirl q to generate the entire AI–CI transition boundary of helical modes $m=\pm 1$ in the $a-q$ plane, as shown in Fig. 5. Moderate amounts of swirl are seen to increase the a-interval leading to AI. As the swirl approaches the stability boundary $q\sim 1.5$ for this particular mode, the range of a-values where AI prevails gradually shrinks, presumably to a point. The present shooting method, however, is unable to track the AI–CI boundary beyond the nearly neutral points marked J and W in Fig. 5 for reasons previously alluded to.

The AI–CI transition curves pertaining to higher-order helical modes $m=-2$ and $m=-3$ may be determined by following the same steps as for $m=\pm 1$. Typical isocontour levels $\omega_i=$const. near a pinching point are displayed in Fig. 6 for $m=-2$, $a_t^j=0.0022$ and $q=0.6$. As in Fig. 4, the Briggs–Bers criterion is clearly satisfied. Computed AI–CI transition boundaries for $m=\pm 1$, $m=-2$ and $m=-3$ have been overlaid in the $a-q$ plane in Fig. 7. This plane may be divided into three distinct regions: A stable (S) domain (with respect to *these modes only* for swirl values above the horizontal line $q\sim 1.5$, an absolutely unstable (AI) bubble, and two convectively unstable (CI) outer-domains located on the jet side and wake side respectively. The AI–CI transition boundary for each m is composed of jet side and wake side curves. The overall AI–CI transition boundary for the Batchelor vortex flow then consists of the "outermost" transition curves pertaining to individual helical modes.

The "state" diagram of Fig. 7 sums up the main results and, as such, deserves to be commented on in detail. In the absence of swirl ($q=0$), the fully developed Gaussian axial velocity profile (1) undergoes a transition to AI with respect to $m=\pm 1$ for a sufficiently strong counterflow $-0.825<a<-0.371$. The application of a moderate amount of swirl

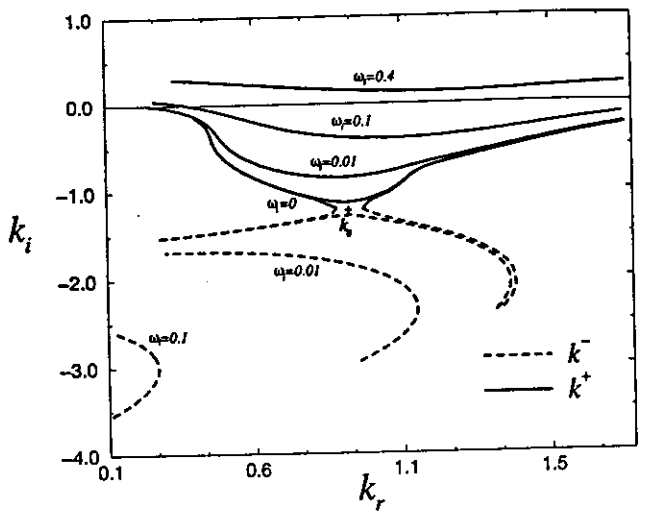

FIG. 6. Illustrative loci of spatial branches $k(\omega)$ in complex k- plane for $m=-2$, $a=a_t^j=0.0022$, $q=0.6$. Level curves $\omega_i=0.4$, $\omega_i=0.1$, $\omega_i=0.01$, $\omega_i=0.0$. Solid lines: $k^+(\omega)$; dashed lines: $k^-(\omega)$. Note pinching of k^+ and k^- branches at k_0 as ω_i decreases to zero.

$0<q<0.7$ is seen to promote absolute instability by significantly increasing the a-interval over which AI takes place. For higher swirl levels $q>0.7$, the AI domain gradually shrinks as q exceeds about 1.5. The mode of transition to AI is significantly different on the wake and jet sides.

On the wake side ($a<-0.5$), the critical transitional mode is always $m=-1$. As soon as the swirl exceeds $q=0.135$, AI may take place *even for co-flowing wakes* $a<-1$.

On the jet side ($a>-0.5$), the critical transitional mode is quite sensitive to swirl and it may have different azimuthal wave numbers $m=-1,-2,-3$. When $q\to 0$, AI takes place *via* the $m=-1$ mode, as in the zero-swirl case. When

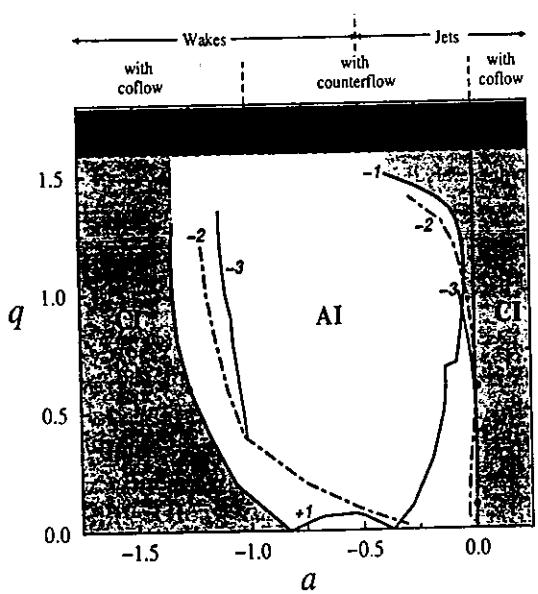

FIG. 7. AI–CI nature of the instability for the Batchelor vortex. Domains of stability (S), convective instability (CI), and absolute instability (AI) in $a-q$ parameter plane. AI–CI transition curves for helical modes $m=\pm 1$, $m=-2$ and $m=-3$ are labeled on the figure. Shaded region indicates outermost boundary of AI region.

$0<q<0.5$, the mode $m=-3$ becomes critical, whereas, for $0.5<q<0.7$, it is replaced by $m=-2$. When $q>0.7$, the mode $m=-1$ is again critical. Note that, in the range $0.134<q<0.704$, the Batchelor vortex jet may be AI even when $a\geqslant 0$, i.e., *for co-flowing jets.*

According to Fig. 7, AI is, for the most part, circumscribed to negative helical modes. When $q=0$, positive and negative helical modes cannot be differentiated: they exhibit identical instability characteristics as a result of the reflectional symmetry $\theta\to-\theta$. When $q\neq 0$, the reflectional symmetry is broken and AI preferentially occurs for $m<0$. This feature is fully consistent with the temporal instability results of Lessen *et al.*[5] and Mayer and Powell[25]: According to these studies, only negative helical modes remain unstable at moderate values of q. As seen from Fig. 7, the only positive helical mode undergoing AI in the presence of a small but finite positive swirl is $m=+1$. As q increases above 0.08, the pocket of AI for $m=+1$ disappears and this mode is never critical in triggering CI–AI transition except for $q=0$.

Finally, note that the AI–CI transition curve for $m=1$ and $q>0$ (solid line labeled $a_t^w Fa_t^j$ in Fig. 5) is the mere reflection with respect to the a axis, of its counterpart for $m=-1$ and $q<0$ (dashed line labeled $a_t^w Ea_t^j$ in Fig. 5). This property follows from the invariance of the dispersion relation under the transformation $q\to-q$ and $m\to-m$.

The loci of the complex absolute wave number k_0 and associated critical point(s) r_c, as q and a vary along the AI–CI transition curves, are displayed in Figs. 8(a), 8(b), 9(a), 9(b), 10(a), and 10(b) for helical modes $m=-1,-2$, and -3, respectively. The swirl q has been selected as the parameter along each AI–CI transition curve and its value appears next to each point of the plots.

Consider first the case of the $m=-1$ mode. As (a,q) moves along the $m=-1$ AI–CI transition curve WEF_1F_2J of Fig. 5, the complex absolute wave number k_0 follows the paths that are similarly labelled in Fig. 8(a). Empty circles refer to the portion WEF_1 and full circles to the portion F_2J. The trajectory of k_0 remains smooth over the part WEF_1, but as (a,q) changes from F_1 to F_2 in Fig. 5, the pinching point k_0 of Fig. 8(a), is seen to experience a sharp jump in location. This unusual feature has been explored in detail and it is further documented in Sec. IV, in connection with the spatial instability characteristics. When the (a,q) setting changes from F_1 to F_2 in Fig. 5, i.e., as the swirl varies from $q=0.68$ to $q=0.70$, it is observed that two neighboring k^+-branches meet at a resonance point and subsequently switch to become two new hybrid k^+-branches. One of the hybrid k^+-branches then pinches at F_2 ($q=0.70$) with a k^--branch. This pinching point labeled F_2 in Fig. 8(a) qualifies as an absolute wave number and it is located a finite distance away from its counterpart at F_1. As (a,q) travels from F_2 to J, the absolute wave number follows again a smooth trajectory, as indicated by the full circles in Fig. 8(a). Finally, note that the three points W,E, and J give rise to nearly neutral modes with $k_{0,i}\ll 1$. There is always a single critical point for the $m=-1$ mode, as represented in Fig. 8(b). The discontinuity in the r_c-trajectory as the swirl crosses the value $q=0.8$ is only apparent. As shown in the

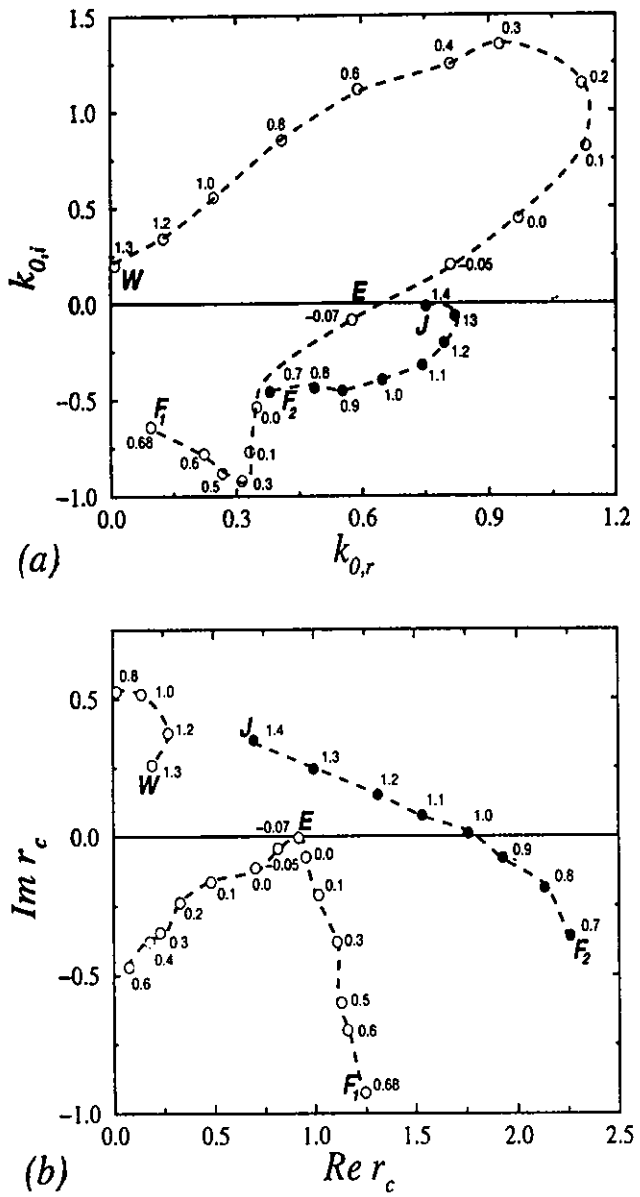

FIG. 8. Helical mode $m=-1$. (a): Locus of absolute wave number k_0 as q and a travel along AI–CI transition curve of Fig. 5. (b): Locus of critical point r_c as q and a travel along AI–CI transition curve of Fig. 5. WEF_1 (○) and F_2J (●) portions of trajectory. Number next to each point refers to corresponding value of swirl q.

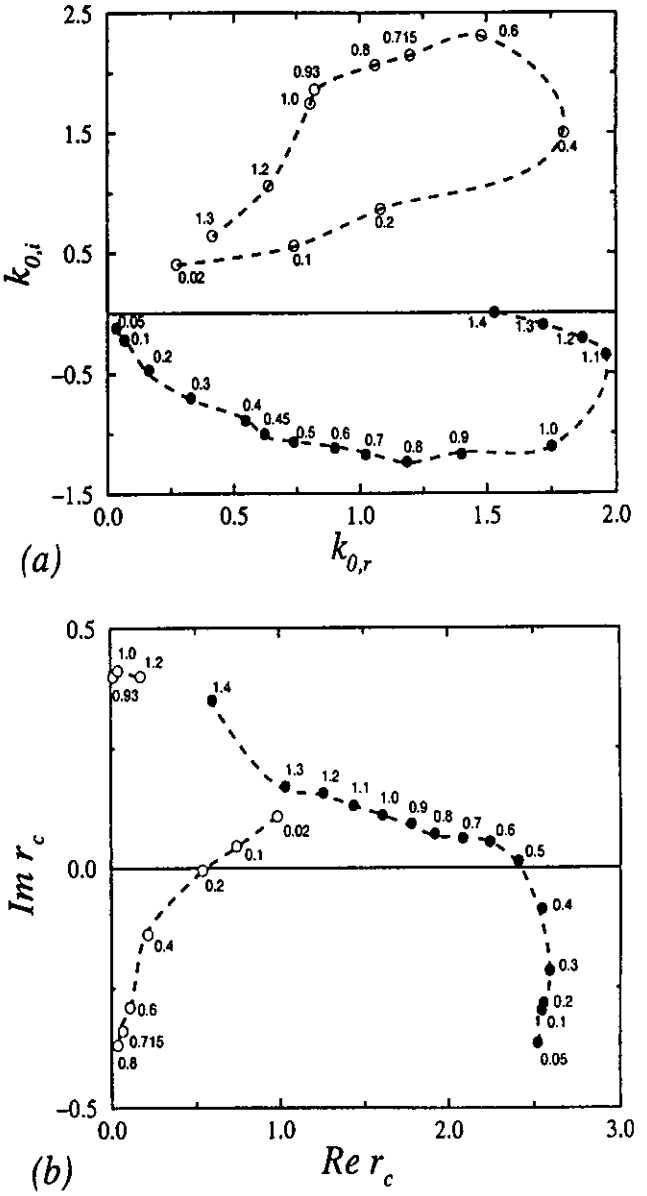

FIG. 9. Helical mode $m=-2$. (a): Locus of absolute wave number k_0 as q and a travel along AI–CI transition curve of Fig. 7. (b): Locus of critical point r_c as q and a travel along AI–CI transition curve $m=-2$ of Fig. 7. "Wake" side (○) and "jet" side (●) portions of trajectory. Number next to each point refers to corresponding value of swirl q.

Appendix, the critical point equation $\gamma(r)=0$ may be written in the form $\Gamma(r^2)=0$. Thus roots come into pairs $(r_c, -r_c)$. Since we have assumed $\mathrm{Re}\, r_c \geq 0$, one must switch from r_c to $-r_c$, as r_c approaches the vertical axis $\mathrm{Re}\, r_c = 0$. This feature accounts for the jump along the path WEF_1 in Fig. 8(b).

The k_0 and r_c-trajectories pertaining to the $m=-2$ and $m=-3$ modes are represented in Figs. 9(a), 9(b), 10(a), and 10(b). Empty circles refer to the wake side and full circles to the jet side of the AI–CI transition curves in Fig. 7. The loci of k_0 do not display any particular feature. The $m=-2$ helical mode always admits a single critical point as shown in Fig. 9(b). For $m=-3$, a single critical point is present on the jet side but two distinct critical points $r_{c,1}$ and $r_{c,2}$ coexist on the wake side of the AI–CI transition curve, as seen in Fig. 10(b).

The existence of two critical points for the $m=-3$ mode on the wake side is further illustrated by the spatial instability results presented in Fig. 11. The flow is taken to be a co-flowing wake at $a=-1.05$ and $q=0.7$, which is located on the CI side of the transition curve for $m=-3$ in Fig. 7. The spatial amplification rate k_i^- of the downstream branch $(x<0)$ is plotted as a function of real frequency ω in Fig. 11(a). The loci of the associated critical points $r_{c,1}$ and $r_{c,2}$, as ω varies, are displayed in Figs. 11(b) and 11(c), respectively.

In all cases, the contour deformation rule was systematically enforced, according to the prescription stated in Sec. II C.

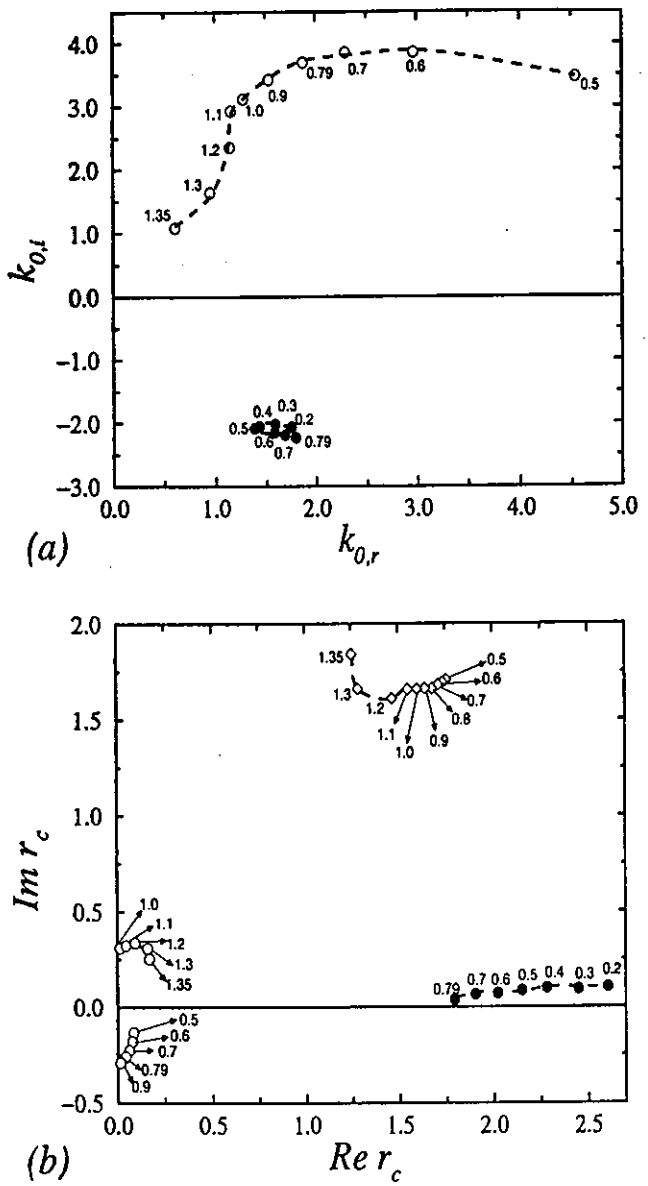

FIG. 10. Helical mode $m=-3$. (a): Locus of absolute wave number k_0 as q and a travel along AI–CI transition curve of Fig. 7. (b): Locus of critical point r_c as q and a travel along AI–CI transition curve $m=-3$ of Fig. 7. "Wake" side (○) and "jet" side (●) portions of trajectory. Number next to each point refers to corresponding value of swirl q.

IV. SPATIAL INSTABILITY OF ZERO EXTERNAL FLOW SWIRLING JETS

In this section, we choose to illustrate the spatial instability characteristics (k complex, ω real) by examining the case of zero-external-flow ($a=0$) swirling jets. Attention is restricted to downstream k^+-branches which are the only ones to become spatially amplified ($-k_i^+>0$) in a finite frequency range. As discussed in the introduction, the axisymmetric mode $m=0$ is known to be always stable whatever the value of q, and only negative helical modes remain unstable at moderate values of q. In the following, we determine the effect of increasing swirl q on the first three negative helical modes $m=-1,-2,-3$. Please note that for given swirl settings higher-order negative helical modes may reach larger amplification rates than the first three modes, as

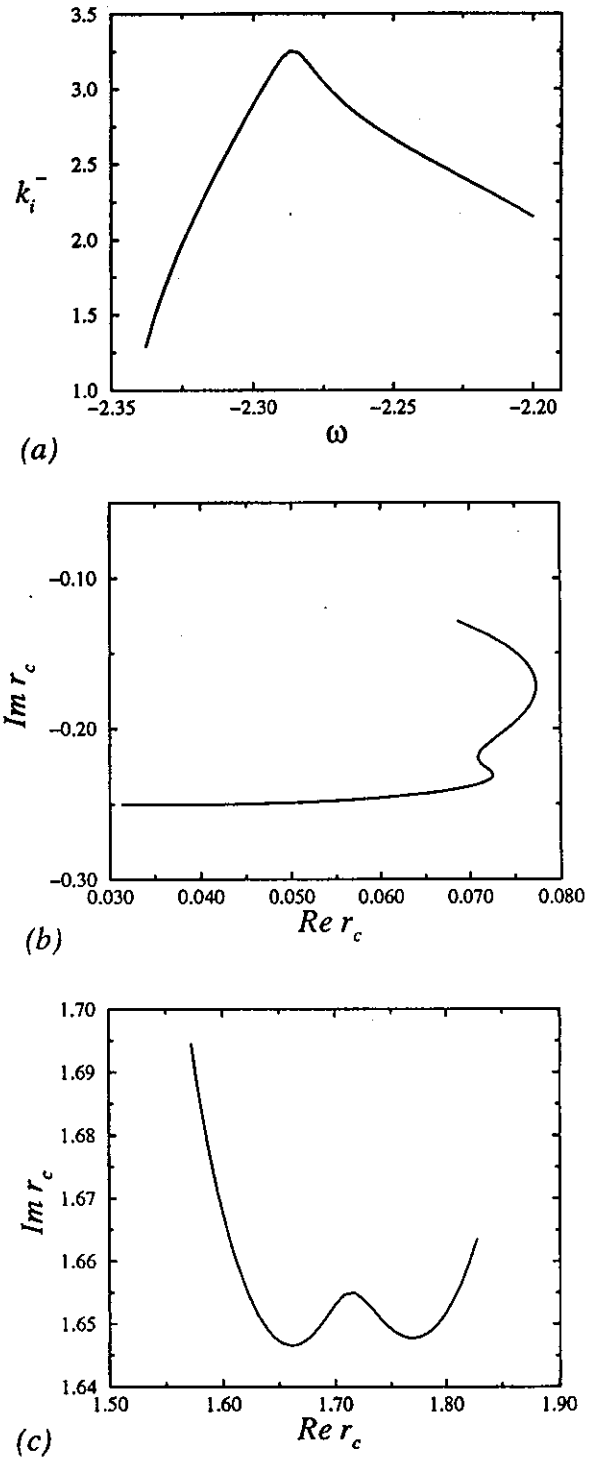

FIG. 11. Helical mode $m=-3$, co-flowing wake at $a=-1.058$, $q=0.7$. Example of k^--spatial branch with two distinct critical points $r_{c,1}$ and $r_{c,2}$. (a): Spatial growth rate k_i^- versus real frequency ω; (b): Locus of critical point $r_{c,1}$ with varying ω; (c): Locus of critical point $r_{c,2}$ with varying ω.

shown by Lessen *et al.*,[5] Mayer and Powell,[25] and Delbende *et al.*[1] Furthermore, Leibovich and Stewartson[27] have demonstrated that the maximum growth rate increases with $|m|$ and tends to a value which is velocity profile dependent. Growth rate trends with increasing swirl q are, however, qualitatively similar for all $m<0$.

The evolution with increasing swirl q, of the spatial amplification rate $-k_i^+$ and real part of the wave number k_r^+,

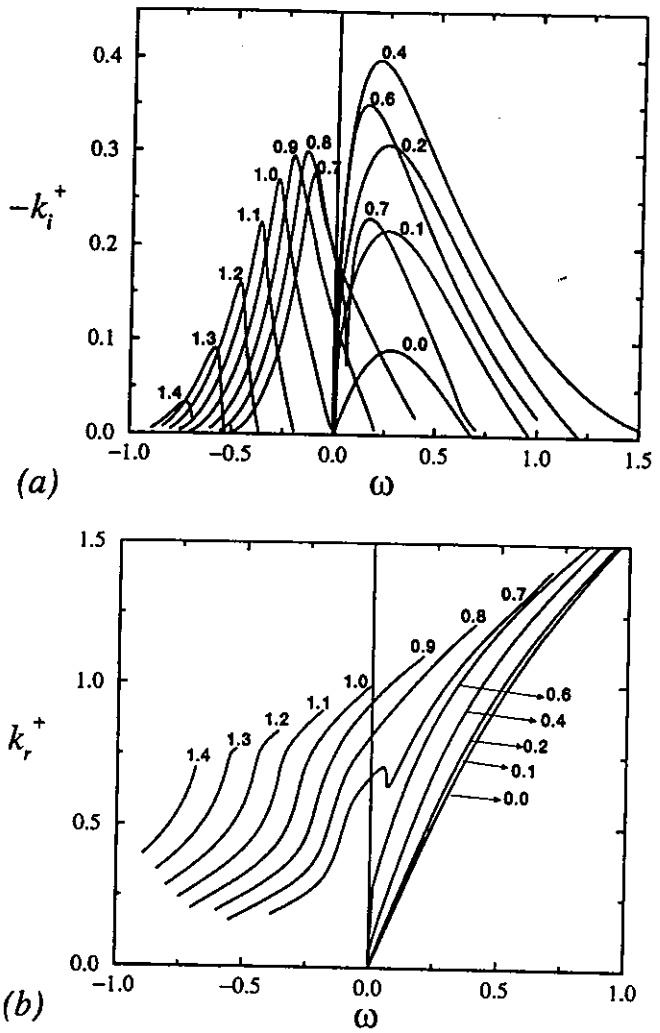

FIG. 12. Helical mode $m=-1$, zero-external-flow swirling jet $a=0$. Evolution of spatial instability characteristics with increasing swirl q. (a): Spatial growth rate $-k_i^+$ versus real frequency ω; (b): Real part of wave number k_r vs ω. Swirl value q is indicated next to each curve.

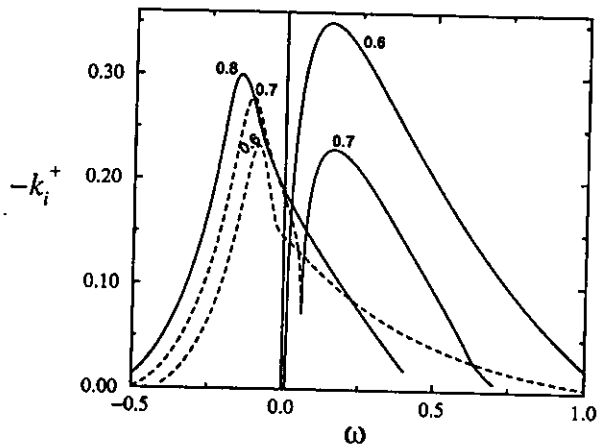

FIG. 13. Helical mode $m=-1$, zero-external-flow swirling jet $a=0$. Spatial growth rate $-k_i^+$ vs frequency ω. Interaction of two spatial branches $k_1^+(\omega)$ (solid line) and $k_2^+(\omega)$ (dashed line) as q increases through 0.7. Swirl value q is indicated next to each curve.

has been documented for helical modes $m=-1$ (Figs. 12 and 13), $m=-2$ (Fig. 14) and $m=-3$ (Fig. 15).

As seen from Fig. 12(a), the helical mode $m=-1$ is unstable for zero swirl and so is $m=1$. These are the only unstable modes for $q=0$. As swirl increases to $q=0.4$, $m=-1$ becomes further destabilized, while increasing swirl beyond $q=0.4$ leads to an overall decrease in spatial amplification rates. The bending mode $m=+1$ (not shown) is stabilized by minute amounts of swirl $q\sim 0.08$. Recall that, for each m, there are infinitely many spatial branches. The spatial branch displayed in Fig. 12 has been obtained by continuation from the temporal mode $m=-1$ identified by Lessen *et al.*,[5] and it is the most amplified for moderate amounts of swirl. However, as q increases from 0.6 to 0.8, this spatial branch experiences a sudden metamorphosis: Note in particular that at $q=0.7$, according to Figs. 12(a) and 12(b) $-k_i^+$ and k_r^+ no longer vanish at the origin as ω tends to zero. In order to understand this feature, let us follow the fate of the spatial branches k_1^+ and k_2^+, indicated by a solid and dashed line, respectively, in Fig. 13. As q reaches 0.7, k_1^+ and k_2^+ actually switch to become two new hybrid k^+-branches which persists for higher q. Only the most amplified hybrid mode at $q=0.8$ has been represented in Fig. 13. This event persists for nonzero a as discussed in the determination of the AI–CI transition curve of the $m=-1$ mode in Sec. IV. Finally, it should be emphasized that, according to Fig. 5, the $m=-1$ mode remains CI on the $a=0$ axis for arbitrarily large swirl levels q: the k^+ spatial instability properties documented in Figs. 12 and 13 effectively characterize the downstream response ($x>0$) of the Batchelor vortex to a time-harmonic excitation of frequency ω.

Corresponding results are shown in Figs. 14 and 15 for the $m=-2$ and $m=-3$ mode, respectively. The helical mode $m=-2$, which is stable for zero swirl $q=0$, experiences a drastic increase in spatial growth rate as q approaches 0.5. The cusp appearing at $q=0.5$ indicates a transition from CI to AI which is consistent with the results of Sec. III: As seen from the state diagram of Fig. 7, the Batchelor vortex with zero external flow $a=0$ becomes AI to the $m=-2$ mode in the range $0.5\leqslant q\leqslant 0.7$. The signalling problem is then ill-posed: Spatial instability branches (dashed lines in Fig. 14) lose their physical significance in the sense that they do not describe the response of the flow to a time-harmonic localized excitation. As q exceeds 0.7, the mode $m=-2$ returns to CI and increasing swirl has a stabilizing influence. Similar features prevail for $m=-3$, as indicated in Fig. 15. The helical mode $m=-3$, which is stable for $q=0$, is destabilized by swirl as q increases to 0.2. In the range $0.2\leqslant q\leqslant 0.5$ (see Fig. 7), the flow is AI to $m=-3$ and spatial branches (dashed lines in Fig. 15) are meaningless. Finally, as q increases above 0.5, the flow returns to CI and the $m=-3$ mode becomes gradually less unstable.

V. SPATIAL EIGENFUNCTIONS

In order to confirm the validity and accuracy of the present numerical method, the computed eigenfunctions have been compared in Fig. 16 with those calculated by Duck and Khorrami[43] for a neutral mode at $m=1$, $a=0$, $q=0.7$, $\omega=0.0425$, and $k=0.6$. In both instances the normalization

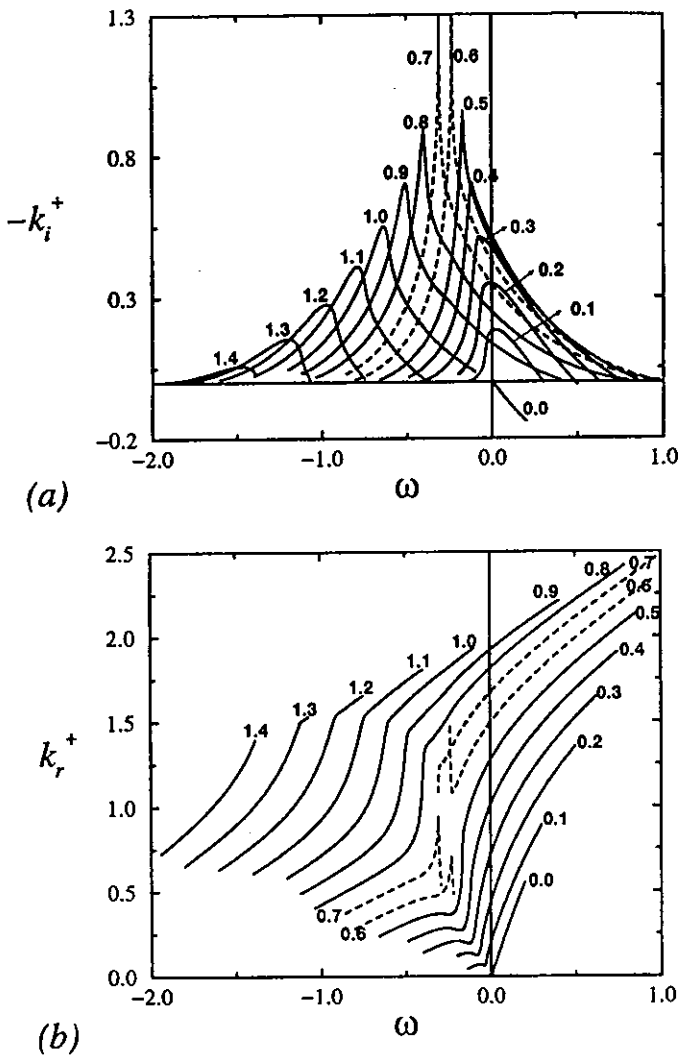

FIG. 14. Helical mode $m=-2$, zero-external-flow swirling jet $a=0$. Evolution of spatial instability characteristics with increasing swirl q. (a): Spatial growth rate $-k_i^+$ versus real frequency ω; (b): Real part of wave number k_r vs ω. Swirl value q is indicated next to each curve. Dashed lines correspond to AI range of q.

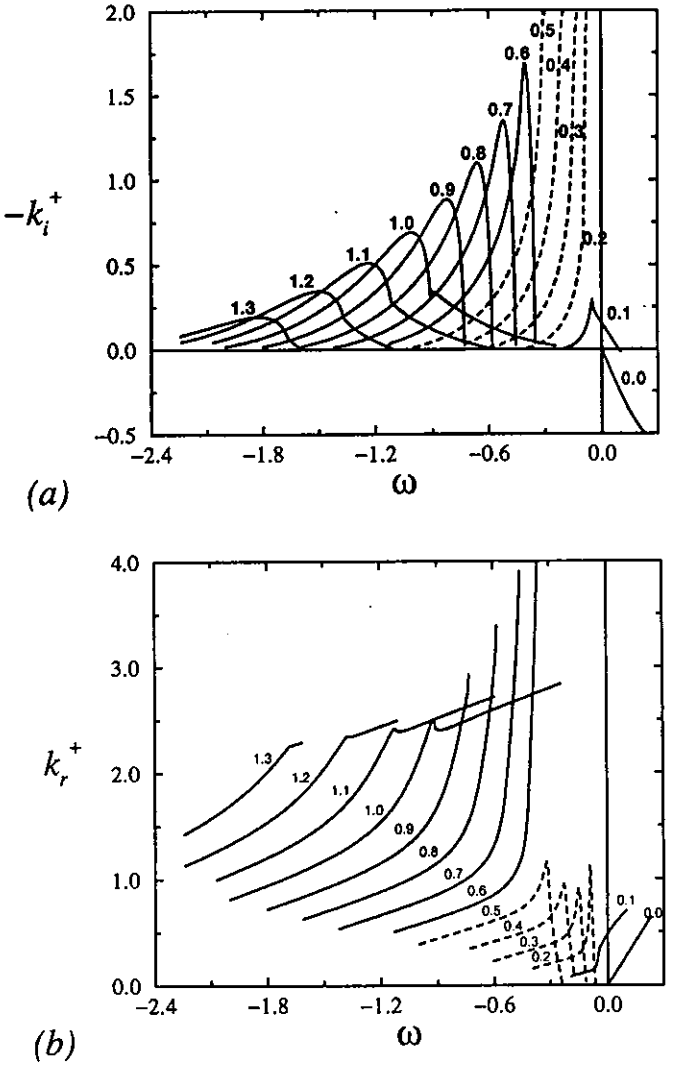

FIG. 15. Helical mode $m=-3$, zero-external-flow swirling jet $a=0$. Evolution of spatial instability characteristics with increasing swirl q. (a): Spatial growth rate $-k_i^+$ vs real frequency ω; (b): Real part of wave number k_r vs ω. Swirl value q is indicated next to each curve. Dashed lines correspond to AI range of q.

condition $G(0)=1$ has been selected. Excellent agreement is obtained. One should mention, however, the presence of a critical point at $r_c=4.058$, outside the range represented in Fig. 16, which induces in its vicinity large variations in the eigenfunction derivatives. Note that $P(r)$ is nearly zero over all radial distances.

Three typical sets of spatial eigenfunctions amplitudes are represented in Fig. 17. The normalization condition has been specified by requiring that the maximum–maximorum over all radial distances and for all $|F|$, $|G|$, $|H|$, and $|P|$ be unity. The selected eigenfunctions are associated with convectively unstable flow conditions indicated by the three full circles in Fig. 7. Figure 17(a) refers to the most amplified downstream k^--wave for the $m=-1$ mode of a *co-flowing wake* ($a=-1.268$), just outside the corresponding CI–AI transition curve of Fig. 7. Figure 17(b) pertains to the most amplified downstream k^+-wave for the $m=-1$ mode of a *co-flowing jet* ($a=0.01$), just outside the corresponding CI–AI transition curve of Fig. 7. Finally, Fig. 17(c) is asso-

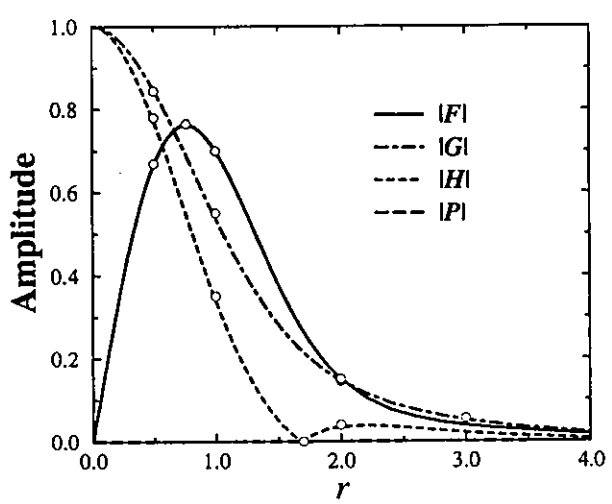

FIG. 16. Eigenfunction amplitudes $|F(r)|$, $|G(r)|$, $|H(r)|$, and $|P(r)|$ for neutral mode at $m=1$, $a=0$, $q=0.7$, $\omega=0.0425$, and $k=0.6$, with normalization condition $G(0)=1$. Continuous or dashed lines: Present approach; (○) inviscid results obtained by Duck and Khorrami (Ref. 43).

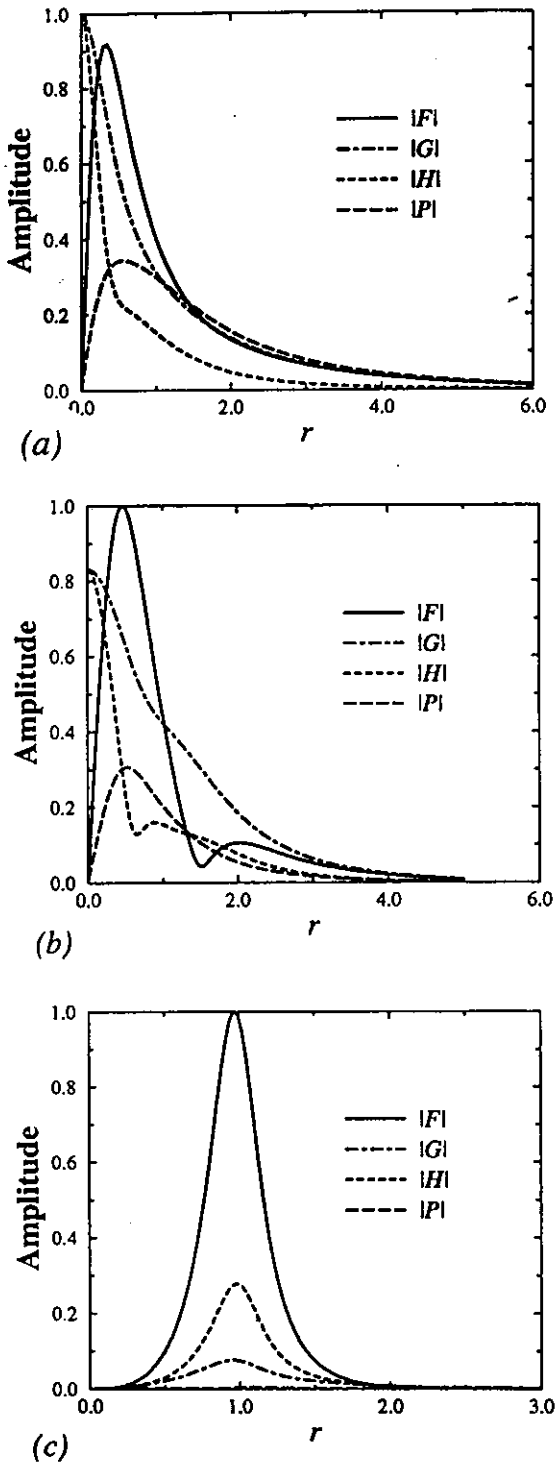

FIG. 17. Spatial eigenfunction amplitudes $|F(r)|$, $|G(r)|$, $|H(r)|$, and $|P(r)|$. (a): Co-flowing wake, $m=-1$, $a=-1.268$, $q=0.6$, most amplified downstream k^--spatial wave at $\omega=-0.78$, $k=(0.454,1.276)$, $r_c=(0.065, -0.485)$. (b): Co-flowing jet $m=-1$, $a=0.01$, $q=0.6$, most amplified downstream k^+-spatial wave at $\omega=0.2$, $k=(0.761,-0.336)$, $r_c=(0.622, -0.528)$. (c): Zero-external flow jet $m=-3$, $a=0$, $q=0.1$, most amplified downstream k^+-spatial wave at $\omega=0.01$, $k=(0.506,-0.139)$, $r_c=(1.005, -0.283)$.

ciated with the most amplified downstream k^+-wave, for the $m=-3$ helical mode of a *zero external flow swirling jet* on the vertical axis of Fig. 7. For all three selected eigenfunctions, the critical point is located well into the lower half r plane, as indicated in the figure caption and the real r axis was chosen as integration path, as sketched in Fig. 2(a).

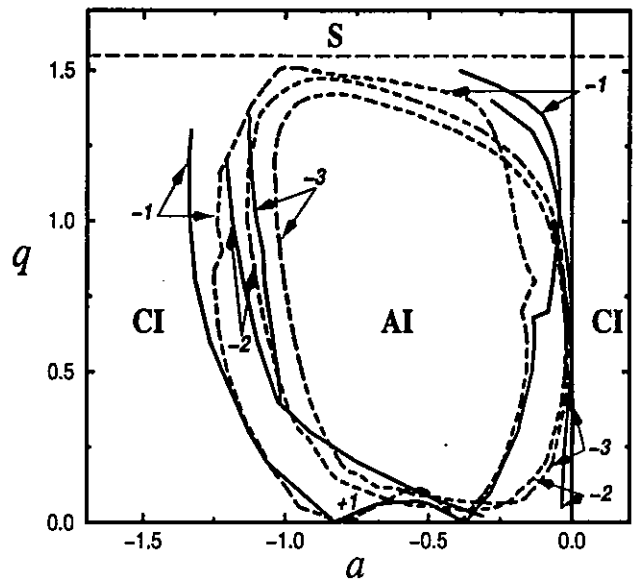

FIG. 18. AI–CI transition curves for azimuthal wave numbers $m=\pm 1$, $m=-2$ and $m=-3$. Dashed lines: results of Delbende *et al.* (Ref. 1) for Re=667. Solid lines: Present inviscid investigation. Number next to curves refers to the azimuthal wave number.

VI. CONCLUDING REMARKS

The main results of the inviscid instability analysis are summarized in Fig. 7. Swirl is seen to promote absolute instability by greatly extending the range of external flow parameters over which AI prevails. The transitional helical mode is very sensitive to the wake-like or jet-like nature of the flow as well as to the level of swirl. On the wake side ($a<-0.5$), the transitional mode is always $m=-1$, which is fully consistent with the results of Monkewitz[44] for bluff body wakes, whereas on the jet side ($a>-0.5$), it successively takes the values $m=-1,-3,-2,-1$ as q is gradually increased. Note that higher-order helical modes ($|m|>3$) may slightly shift the AI–CI outer boundary, as documented by Delbende *et al.*[1] Co-flowing wakes $a<-1$ may become AI as soon as the swirl exceeds $q=0.135$. Similarly, co-flowing jets ($a>0$) may become AI for swirl levels in the range $0.134<q<0.704$.

The AI–CI transition curves of this study have been derived by applying the zero-group velocity criterion of Briggs[13] and Bers,[14] directly to the *inviscid* dispersion relation (9). In Fig. 18, these results have been compared with those obtained in Delbende *et al.*[1] by applying a suitable decomposition procedure to the computed viscous linear impulse response at the finite Reynolds number Re $=(\Delta UR/\nu)=667$. A blow-up of the transition curves in the vicinity of zero-external flow jet axis $a=0$ is presented in Fig. 19. Both sets of curves are in good qualitative and quantitative agreement. Finite viscous effects are seen to lead to a slight contraction of the pocket of absolute instability, especially near the upper stability boundary where viscous diffusion is likely to stabilize modes that are only weakly unstable on an inviscid basis. In particular, viscosity at Re=667 is

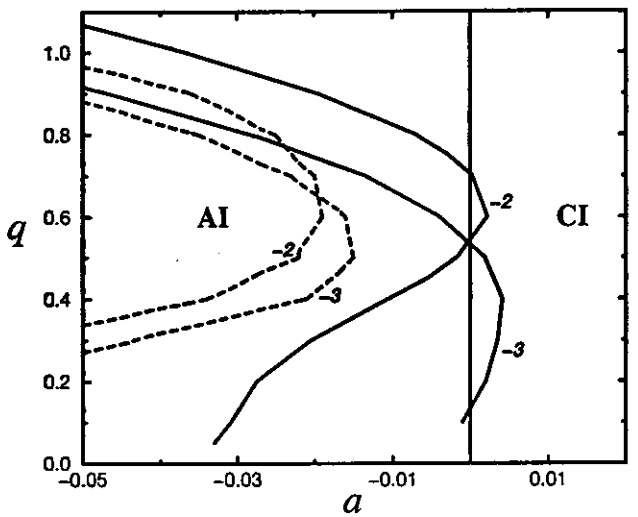

FIG. 19. Magnification near $a=0$ of the transition curves for $m=-2$ and $m=-3$ displayed in Fig. 18. Dashed lines: Results of Delbende *et al.* (Ref. 1) for Re=667. Solid lines: Present inviscid investigation. Number next to curves refers to the azimuthal wave number.

seen to be sufficient to push the inviscid AI–CI transition curves on the jet side ($a>0$) slightly to the left, into the half-plane $a<0$. As a consequence, co-flowing jets ($a>0$) are no-longer capable of sustaining an absolute instability at Reynolds numbers of the order of 667. By contrast, co-flowing wakes ($a<-1$) remain absolutely unstable for sufficiently large swirl at Re=667. The numerical method used in the present work presents both advantages and disadvantages when compared with the impulse response decomposition procedure of Delbende *et al.*[1] The shooting method leads to very accurate results which are in excellent agreement with those of Duck and Khorrami,[43] but convergence relies heavily on the availability of realistic guess values, such as those generated by the impulse response calculations of Delbende *et al.*![1] In near-neutral situations, where many modes are expected to coalesce, the shooting method experiences convergence difficulties.

The results of the present investigation may also be compared with the inviscid instability analysis of the Rankine vortex with axial flow recently performed by Loiseleux *et al.*[6] As readily seen by comparing Fig. 7 with Fig. 20 of Loiseleux *et al.*,[6] the overall shapes of the AI regions in the $a-q$ plane are qualitatively similar. In both instances, counterflow does not remain a prerequisite for AI at sufficiently high swirl levels. For moderate swirl, the transitional mode on the wake side ($a<-0.5$) is $m=-1$ for both basic flows. On the jet side ($a>-0.5$), AI of the Rankine vortex may be induced through various negative helical modes, as for the Batchelor vortex. The AI region for the Rankine vortex remains open on the high q-side. According to the *viscous* calculations of Delbende *et al.*,[1] the AI region for the Batchelor vortex is closed above $q\sim 1.5$. There remains to establish whether this feature persist in the inviscid limit. The present study has not conclusively settled this question. Finally, the Rankine vortex undergoes AI on the jet side at very low q through the axisymmetric mode $m=0$. This possibility is obviously ruled out in the case of the Batchelor vortex, since it remains stable to axisymmetric disturbances.

According to several theoretical investigations (Chomaz *et al.*,[19] Monkewitz *et al.*,[45] LeDizès *et al.*[20]), the existence of a finite pocket of absolute instability in spatially developing shear-flows is known to favor the onset of self-sustained oscillations or so-called global modes. In this regard, the present work provides further support for the conjecture made by Delbende *et al.*[1]: The application of swirl provides an efficient means of promoting global mode onset in wakes and jets. In jets, swirl is likely to lead to preferential selection of a variety of helical patterns $m=-1,-2,-3$. In wakes, the bending mode $m=-1$ should be singled out.

ACKNOWLEDGMENTS

The authors are very grateful to Ivan Delbende and Thomas Loiseleux for many fruitful and helpful discussions. They are indebted to an anonymous Referee for helpful suggestions in revising the manuscript. Financial support was provided by Grant No. 92-098 of the Direction des Recherches, Études et Techniques (DRET) of the French Ministry of Defense.

APPENDIX

The objective of this appendix is to prove that the critical point equation $\gamma(r)=0$ given by (1) and (5) admits at most two nonzero complex roots with $\mathrm{Re}\, r\geqslant 0$ as soon as $mq\neq 0$. The same statement is true when $mq=0$. provided that $(k,\omega)\neq(0,0)$.

Upon making the change of variable $u=r^2$, Eq. (5) may be written as

$$\Gamma(u)\equiv-\omega+k[a+e^{-u}]+\frac{mq}{u}(1-e^{-u})=0. \tag{A1}$$

Assume that, for a given pair (k,ω), there exist three distinct nonzero complex roots u_1, u_2, u_3 of Eq. (A1). In such a case, the complex pair (k,ω) satisfies the set of linear equations

$$\omega-k[a+e^{-u_1}]=\frac{mq}{u_1}(1-e^{-u_1}), \tag{A2}$$

$$\omega-k[a+e^{-u_2}]=\frac{mq}{u_2}(1-e^{-u_2}), \tag{A3}$$

$$\omega-k[a+e^{-u_3}]=\frac{mq}{u_3}(1-e^{-u_3}). \tag{A4}$$

Since $u_1\neq u_2$, Eqs. (A2), and (A3) may readily be solved for k and ω to yield

$$k=k(u_1,u_2)=\frac{mq[(1-e^{-u_2})u_2^{-1}-(1-e^{-u_1})u_1^{-1}]}{e^{-u_2}-e^{-u_1}}, \tag{A5}$$

$$\omega=\omega(u_1,u_2)=k(u_1,u_2)(a+e^{-u_1})+\frac{mq}{u_1}(1-e^{-u_1}). \tag{A6}$$

If $mq \neq 0$, then, according to Eq. (A5), $k \neq 0$. The pair (k,ω) specified in (A5) and (A6) also satisfies Eq. (A4) provided that

$$a+e^{-u_3}=a+e^{-u_1}, \quad (1-e^{-u_3})u_1=(1-e^{-u_1})u_3. \qquad \text{(A7)}$$

These conditions necessarily imply that $u_1=u_3$. Thus, the equation $\Gamma(u)=0$ admits at most two distinct roots u_1 and u_2. Since $u=r^2$, the original critical point equation $\gamma(r)=0$ also admits at most two distinct roots $r_{c,1}$ and $r_{c,2}$ with $\mathrm{Re}\, r \geqslant 0$.

Consider now the case $mq=0$. According to Eqs. (A5) and (A6), one necessarily has $(k,\omega)=(0,0)$ and the system (A2)–(A4) is then identically satisfied. If one insists that $(k,\omega)\neq(0,0)$, Eq. (A1) has at most one root, which concludes the proof.

[1] I. Delbende, J. M. Chomaz, and P. Huerre, "Absolute/convective instabilities in the Batchelor vortex: a numerical study of the linear impulse response," J. Fluid Mech. **355**, 229 (1998).

[2] R. L. Ash and M. R. Khorrami, "Vortex stability," in *Fluid Vortices*, edited by Sheldon I. Green (Kluwer Academic, Dordrecht, 1995), pp. 317–372.

[3] M. Lessen and F. Paillet, "The stability of a trailing line vortex. Part 2. Viscous theory," J. Fluid Mech. **65**, 769 (1974).

[4] M. Lessen and P. J. Singh, "The stability of axisymmetric free shear layers," J. Fluid Mech. **60**, 433 (1974).

[5] M. Lessen, P. J. Singh, and F. Paillet, "The stability of a trailing line vortex. Part 1. Inviscid theory," J. Fluid Mech. **63**, 753 (1974).

[6] T. Loiseleux, J. M. Chomaz, and P. Huerre, "The effect of swirl on jets and wakes: Linear instability of the Rankine vortex with axial flow," Phys. Fluids **10**, 1120 (1998).

[7] T. J. Pedley, "On the instability of rapidly rotating shear flows to non-axisymmetric disturbances," J. Fluid Mech. **31**, 603 (1968).

[8] T. J. Pedley, "On the instability of viscous flow in a rapidly rotating pipe," J. Fluid Mech. **35**, 97 (1969).

[9] J. E. Martin and E. Meiburg, "Nonlinear axisymmetric and three-dimensional vorticity dynamics in a swirling jet model," Phys. Fluids **8**, 1917 (1996).

[10] G. K. Batchelor, "Axial flow in trailing line vortices," J. Fluid Mech. **20**, 645 (1964).

[11] P. Huerre and P. A. Monkewitz, "Local and global instabilities in spatially developing flows," Annu. Rev. Fluid Mech. **22**, 473 (1990).

[12] P. Huerre and M. Rossi, "Hydrodynamic instabilities in open flows," in *Hydrodynamics and Nonlinear Instabilities*, edited by C. Godrèche and P. Manneville (Cambridge University Press, Cambridge, 1998), pp. 81–294.

[13] R. G. Briggs, *Electron-Stream Interaction with Plasmas* (Cambridge University Press, Cambridge, 1964).

[14] A. Bers, "Space-time evolution of plasma instabilities–absolute and convective," in *Handbook of Plasma Physics*, edited by M. N. Rosenbluth and R. Z. Sagdeev (North- Holland, Amsterdam, 1983), Vol. I, p. 451.

[15] C. Olendraru, A. Sellier, M. Rossi, and P. Huerre, "Absolute/convective instability of the Batchelor vortex," C. R. Acad. Sci., Ser. IIb: Mec., Phys., Chim., Astron. **323**, 153 (1996).

[16] S. Leibovich, "The structure of vortex breakdown," Annu. Rev. Fluid Mech. **10**, 221 (1978),

[17] S. Leibovich, "Vortex stability and breakdown: Survey and extension," AIAA J. **22**, 1192 (1983).

[18] S. Wang and Z. Ruzak, "On the stability of an axisymmetric rotating flow in a pipe," Phys. Fluids **8**, 1007 (1995).

[19] J. M. Chomaz, P. Huerre, and L. G. Redekopp, "A frequency selection criterion in spatially developing flows," Stud. Appl. Math. **84**, 119 (1991).

[20] S. LeDizès, P. Huerre, J. M. Chomaz, and P. A. Monkewitz, "Linear global modes in spatially developing media," Philos. Trans. R. Soc. London, Ser. A **354**, 169 (1996).

[21] J. H. Faler and S. Leibovich, "Disrupted states of vortex flow and vortex breakdown," Phys. Fluids **20**, 1385 (1977).

[22] A. K. Garg and S. Leibovich, "Spectral characteristics of vortex breakdown flowfields," Phys. Fluids **22**, 2053 (1979).

[23] P. G. Sarpkaya, "On stationary and traveling vortex breakdown," J. Fluid Mech. **45**, 545 (1971).

[24] L. N. Howard and A. S. Gupta, "On the hydrodynamic and hydromagnetic stability of swirling flows," J. Fluid Mech. **14**, 463 (1962).

[25] E. W. Mayer and K. G. Powell, "Viscous and inviscid instabilities of a trailing line vortex," J. Fluid Mech. **245**, 91 (1992).

[26] K. Stewartson and S. N. Brown, "Near-neutral center-modes as inviscid perturbations to a trailing line vortex," J. Fluid Mech. **156**, 387 (1985).

[27] S. Leibovich and K. Stewartson, "A sufficient condition for the instability of columnar vortices," J. Fluid Mech. **126**, 335 (1983).

[28] M. R. Khorrami, "On the viscous modes of instability of a trailing line vortex," J. Fluid Mech. **255**, 197 (1991).

[29] T. B. Benjamin, "Theory of the vortex breakdown phenomenon," J. Fluid Mech. **14**, 593 (1962).

[30] C.-Y. Tsai and S. E. Widnall, "Examination of a group-velocity criterion for breakdown of vortex flow in a divergent duct," Phys. Fluids **23**, 864 (1980).

[31] S. Leibovich, S. N. Brown, and Y. Patel, "Bending waves on inviscid columnar vortices," J. Fluid Mech. **173**, 595 (1986).

[32] G. K. Batchelor and A. E. Gill, "Analysis of the stability of axisymmetric jets," J. Fluid Mech. **14**, 529 (1962).

[33] C. M. Bender and S. A. Orszag, *Advanced Mathematical Methods for Scientists and Engineers* (McGraw-Hill, New York, 1978).

[34] P. Huerre and P. A. Monkewitz, "Absolute and convective instabilities in free shear layers," J. Fluid Mech. **159**, 151 (1985).

[35] M. Abramowitz and I. A. Stegun, *Handbook of Mathematical Functions* (Dover, New York, 1965).

[36] C. C. Lin, *Hydrodynamic Stability* (Cambridge University Press, Cambridge, 1955).

[37] W. Wasow, "The complex asymptotic theory of a fourth-order differential equation of hydrodynamics," Ann. Math. **49**, 852 (1948).

[38] P. G. Drazin and W. Reid, *Hydrodynamic Stability* (Cambridge University Press, Cambridge, 1981).

[39] S. Le Dizès, P. A. Monkewitz, and P. Huerre, "Viscous structure of plane waves in spatially developing shear flows," Phys. Fluids **7**, 1337 (1995).

[40] K. M. Case, "Stability of inviscid plane Couette flow," Phys. Fluids **3**, 143 (1960).

[41] S. Pavithran and L. G. Redekopp, "The absolute-convective transition in subsonic mixing layers," Phys. Fluids A **1**, 1736 (1989).

[42] M. R. Khorrami, M. R. Malik, and R. L. Ash, "Application of spectral collocation techniques to the stability of swirling flows," J. Comput. Phys. **81**, 206 (1989).

[43] P. W. Duck and M. R. Khorrami, "A note on the effects of viscosity on the stability of a trailing-line vortex," J. Fluid Mech. **245**, 175 (1992).

[44] P. A. Monkewitz, "A note on vortex shedding from axisymmetric bluff bodies," J. Fluid Mech. **192**, 561 (1988).

[45] P. A. Monkewitz, P. Huerre, and J. M. Chomaz, "Global linear stability analysis of weakly non-parallel shear flows," J. Fluid Mech. **251**, 1 (1993).